A parametric model for reactive high-power impulse magnetron sputtering of films

Tomáš Kozák[1,2] and Jaroslav Vlček[1]

[1]Department of Physics and NTIS – European Centre of Ecellence, University of West Bohemia, Univerzitní 8, 30614 Plzeň, Czech Republic

[2]Department of Chemistry, PLASMANT Research Group, University of Antwerp, Universiteitsplein 1, B-2610 Antwerp, Belgium

E-mail: `vlcek@kfy.zcu.cz`

Abstract. We present a time-dependent parametric model for reactive HiPIMS deposition of films. Specific features of HiPIMS discharges and a possible increase in the density of the reactive gas in front of the reactive gas inlets placed between the target and the substrate are considered in the model. The model makes it possible to calculate the compound fractions in two target layers and in one substrate layer, and the deposition rate of films at fixed partial pressures of the reactive and inert gas. A simplified relation for the deposition rate of films prepared using a reactive HiPIMS is presented. We used the model to simulate controlled reactive HiPIMS depositions of stoichiometric ZrO_2 films, which were recently carried out in our laboratories with two different configurations of the O_2 inlets in front of the sputtered target. The repetition frequency was 500 Hz at the deposition-averaged target power densities of 5 Wcm^{-2} and 50 Wcm^{-2} with a pulse-averaged target power density up to 2 $kWcm^{-2}$. The pulse durations were 50 μs and 200 μs. Our model calculations show that the to-substrate O_2 inlet provides systematically lower compound fractions in the target surface layer and higher compound fractions in the substrate surface layer, compared with the to-target O_2 inlet. The low compound fractions in the target surface layer (being approximately 10 % at the deposition-averaged target power density of 50 Wcm^{-2} and the pulse duration of 200 μs) result in high deposition rates of the films produced, which are in agreement with experimental values.

Submitted to: *J. Phys. D: Appl. Phys.*

1. Introduction

In recent years, high-power impulse magnetron sputtering (HiPIMS) systems have been used for deposition of films (see, for example, [1–3]). The target power density in a pulse of these discharges with a peak value of up to several $\mathrm{kWcm^{-2}}$ is orders of magnitude higher than a typical target power density (usually less than $20\,\mathrm{Wcm^{-2}}$) applied in conventional dc magnetron sputtering. The high target power density leads to generation of very dense discharge plasmas with high degrees of ionization of sputtered atoms. Consequently, film depositions can be carried out at highly ionized fluxes of the target material atoms. This is of significant interest for deposition on complex-shaped substrates[4, 5], for substrate–film interface engineering resulting in enhanced film adhesion [6] and for the preparation of films with dense microstructure and controlled phase composition [4, 5, 7].

HiPIMS systems have been applied in the preparation of various optically transparent non-conductive metal oxides, for example, TiO_2 [8–11], ZrO_2 [12, 13], Ta_2O_5 [12], HfO_2 [13, 14] and Nb_2O_5 [15], of thermochromic VO_2 films [16] and of optically transparent conductive oxides, such as InSnO [17], Al-doped ZnO [18] and RuO_2 [19]. Recently, Hála et al. demonstrated the suitability of reactive HiPIMS for the preparation of high-quality single SiO_2 and Ta_2O_5 optical films as well as for fabrication of optical multilayer stacks[20].

In our recent paper [21], we reported on high-rate reactive depositions of densified, highly optically transparent, stoichiometric ZrO_2 films using HiPIMS with a pulsed reactive gas (oxygen) flow control. An optimized location of two O_2 inlets, which were oriented toward the substrate, made it possible to improve the quality of the films due to minimized arcing at the sputtered target and to enhance their deposition rates up to 120 nm/min at the deposition-averaged target power density of approximately $50\,\mathrm{Wcm^{-2}}$ and the target-to-substrate distance of 100 mm. We have thus demonstrated a great potential of the controlled reactive HiPIMS for high-rate depositions of densified dielectric oxide films onto floating substrates at low substrate temperatures in coating technologies and in microelectronics.

In this paper, we present a time-dependent parametric model for reactive HiPIMS deposition of films. Our strategy was to select a realistic but simple model developed for conventional reactive magnetron sputtering (see, for example, [22–29] and the works cited therein) and to extend its applicability to the specific conditions of HiPIMS discharges. A brief characterization of the models for conventional reactive magnetron sputtering is given in the recent work of Strijckmans and Depla [29].

Our starting point is the model developed by Kubart et al.[27] that takes into account not only the process of chemisorption of reactive gas molecules, as in the case of earlier models [22–26], but also the processes of knock-on and direct implantation of reactive gas atoms and ions, respectively [28–33], resulting in a compound formation at the target.

The processes we considered are the following: Sputtering of metal and reactive gas atoms from the target and their transfer onto the substrate, chemisorption of reactive gas particles on the target and substrate, and knock-on implantation of reactive gas atoms and direct implantation of reactive gas ions and metal ions into the target. The original model equations [27] were significantly modified and supplemented to account for specific features of HiPIMS discharges, namely, gas rarefaction and ionization in front of the sputtered target, high degree of dissociation of reactive gas molecules in the fluxes onto the target and substrate, and backward flux of the ionized sputtered metal atoms and reactive gas atoms onto the target. The effects relating to the backward flux of the ionized sputtered metal atoms onto the target are of key importance for reactive HiPIMS deposition of films. They are described using a phenomenological model for HiPIMS of metals which was developed by Vlček and Burcalová [34] on the basis of the original model of Christie [35].

In contrast with the usual approaches [26, 27, 29], the partial pressure of the reactive gas is not calculated from the balance of the reactive gas in a vacuum chamber. We assume that a process control is used to keep a partial pressure of the reactive gas constant in time during the film deposition. Therefore, we do not have to investigate the compound composition on chamber walls, which is in general different from that on a substrate [23, 29]. On the contrary, we consider the substrate as a plate facing the target at a specified distance of several centimetres from the target surface. Thus, we focus not only on the processes at the target and substrate surfaces, but also on the processes in a discharge plasma between the target and the substrate. Moreover, the model can account for a possible increase in the density of the reactive gas in front of the reactive gas inlets placed between the target and the substrate [21].

We used this model to explain large differences between the deposition rates of the ZrO_2 films achieved using controlled reactive HiPIMS depositions with two different configurations of the O_2 inlets in front of the sputtered target [21]. Moreover, we carried out model calculations to investigate the effects of the specific features of HiPIMS discharges on the processes on the target and the substrate surfaces during the depositions, and on the deposition rates of the ZrO_2 films produced.

2. Description of the model

2.1. Basic model assumptions

Our model for reactive HiPIMS deposition of films has been developed under the following basic assumptions:

(i) The metallic planar magnetron target with the erosion area A_{te} is sputtered uniformly by singly charged ions coming from a plasma of the discharge

Table 1. List of symbols. Subscripts are used to distinguish equivalent variables related to different particles in the plasma or, like superscripts, to different positions in the discharge. We use *t* for target, *te* for target erosion zone, *ts* for target surface layer, *tb* for target bulk layer, *s* for substrate, *rm* for reactive gas molecules, *ra* for reactive gas atoms, *r* for reactive gas, *i* for inert gas, *m* for metal and *c* for compound. Note that the fluxes of particles, $\Gamma_{\rm pr}$, and integral fluxes, $I_{\rm pr}$, have different subscripts in the text with respect to the processes they are related to.

Symbol	Definition
$A_{\rm t}$, $A_{\rm te}$, $A_{\rm s}$	Area
$a_{\rm D}$	Deposition rate of films
$\alpha^{\rm t}_{\rm rm}$, $\alpha^{\rm t}_{\rm ra}$, $\alpha^{\rm s}_{\rm rm}$, $\alpha^{\rm s}_{\rm ra}$	Sticking coefficient
$B_{\rm m}$, $B_{\rm r}$	Probability of ionization and subsequent return of sputtered atoms onto target
$B_{\rm ma}$	Pulse-averaged $B_{\rm m}$
$\beta_{\rm m}$	Probability of ionization of sputtered metal atoms
$\Gamma^{\rm t}_{\rm pr}$, $\Gamma^{\rm s}_{\rm pr}$	Flux of particles
γ	Effective secondary electron emission yield
$D_{\rm t}$, $D_{\rm s}$	Dissociation probability of reactive gas molecules
d	Target-to-substrate distance
e	Elementary charge
$F_{\rm t}$, $F_{\rm s}$	Overfilling factor of reactive gas
$f_{\rm r}$	Fraction of reactive gas ions in the ion flux onto target
$f_{\rm rep}$	Repetition frequency
$f_{\rm trm}$, $f_{\rm trr}$	Transport factor of sputtered atoms
$h_{\rm ts}$, $h_{\rm tb}$, $h_{\rm s}$	Thickness of layer
$I_{\rm d}$	Discharge current
$I_{\rm pr}$	Integral flux of particles
$J_{\rm t}$	Target current density
k	Boltzmann constant
$k_{\rm sp}$	Sputtering yield proportionality constant
$M_{\rm m}$	Molar mass of target material
$M_{\rm s}$	Deposition rate of metal atoms
$m_{\rm rm}$	Mass of a reactive gas molecule
$m_{\rm t}$	Fraction of metal ions in the ion flux onto target
$N_{\rm A}$	Avogadro constant
n_0	Atomic density of metal target
$n_{\rm m,c}$	Atomic density of metal atoms in compound
$p_{\rm i}$, $p_{\rm rm}$	Pressure
$\Phi_{\rm ox}$	Oxygen flow rate
$R_{\rm t}$	Reduction factor due to gas rarefaction and ionization
$R_{\rm rm}$, $R_{\rm rc}$, $R_{\rm mm}$, $R_{\rm mc}$	Backscattering probability of atoms from target
$R_{\rm efr}$, $R_{\rm efm}$	Effective backscattering probability of atoms from target
ρ	Mass density of target material

Table 1. List of symbols (continued).

Symbol	Definition
$\langle S_{\rm d} \rangle$	Deposition-averaged target power density
$S_{\rm da}$	Average target power density in pulse
$\sigma_{\rm m}$	Probability of return of ionized sputtered metal atoms onto target
$T_{\rm g}$	Gas temperature
$T_{\rm p}$	Pulse period
t	Time
$t_{\rm on}$, $t_{\rm ac}$	Pulse-on time, plasma activation after pulse
$\Theta_{\rm ts}$, $\Theta_{\rm tb}$, $\Theta_{\rm s}$	Compound fraction
$\Theta_{\rm tsa}$	Pulse-averaged $\Theta_{\rm ts}$
$U_{\rm d}$	Magnetron voltage
$U_{\rm da}$	Pulse-averaged magnetron voltage
x	Stoichiometry of compound (MO_x)
$Y_{\rm mm}$, $Y_{\rm mc}$, $Y_{\rm rc}$	Sputtering yield
$Y'_{\rm rc}$	Knock-on implantation yield of reactive gas atoms

generated by a high-power pulsed dc power supply at time-varying magnetron voltage, $U_{\rm d}(t)$, and the discharge current, $I_{\rm d}(t)$.

(ii) The uniform films are deposited onto a planar substrate with the area $A_{\rm s}$, facing the target at the distance d from the target surface.

(iii) The discharge gas is a mixture of one inert gas and one diatomic reactive gas with the partial pressures of $p_{\rm i}$ and $p_{\rm rm}$, respectively, which are measured, as usual, at the wall of the vacuum chamber. A local increase in the density of the reactive gas can occur in front of the reactive gas inlets placed between the target and the substrate.

(iv) A process control allows to perform a stable reactive HiPIMS at given values of $p_{\rm i}$ and $p_{\rm rm}$ constant in time.

(v) The effective ion-induced secondary electron emission yield, γ, at the target is independent of the position in the target erosion area as well as of the process parameters $U_{\rm d}(t)$, $I_{\rm d}(t)$, $p_{\rm i}$ and $p_{\rm rm}$.

(vi) The effects of negative reactive gas ions are neglected.

2.2. Model equations

2.2.1. Target surface and bulk layers

A typical thickness of a compound layer in the target erosion area extends up to several nanometres and depends on the energy and type of implanted reactive gas ions [28, 36–38]. In this model, the compound layer in the target erosion area is subdivided into two layers, a surface layer with a thickness $h_{\rm ts}$ of one monolayer (from now on called simply the target surface layer) and a bulk layer with a thickness

h_{tb} given by an implantation depth of the reactive gas ions in the target material (from now on called simply the target bulk layer). This is analogous to the two-layer model of Möller and Güttler [28].

The composition of the target surface layer and the target bulk layer is described by the compound fractions Θ_{ts} and Θ_{tb}, respectively, which represent the portions of the layers consisting of the stoichiometric compound MR_x, where M is a metal atom, R is a reactive gas atom and x is a stoichiometry factor. The complement consists of a non-reacted metal. The equations for the compound fractions Θ_{ts} and Θ_{tb} are formulated as balance equations for the surface density of reactive gas atoms in the target surface layer and the target bulk layer, respectively (see, e.g., [27, 29]).

For the target surface layer, we use the equation

$$n_0 h_{\mathrm{ts}} x \frac{\mathrm{d}\Theta_{\mathrm{ts}}(t)}{\mathrm{d}t} = \Gamma^{\mathrm{t}}_{\mathrm{ch}}(t) + \Gamma^{\mathrm{t}}_{\mathrm{exp}}(t) + \Gamma^{\mathrm{t}}_{\mathrm{disr}}(t) - \Gamma^{\mathrm{t}}_{\mathrm{spr}}(t) - \Gamma^{\mathrm{t}}_{\mathrm{kir}}(t) \,, \qquad (1)$$

where n_0 is the atomic density of the target material before reaction and the terms on the right-hand side of equation (1) represent the fluxes of particles (in particles per cm^2 per second) increasing and decreasing the content of reactive gas atoms in the target surface layer. Here, $\Gamma^{\mathrm{t}}_{\mathrm{ch}}(t)$ is the chemisorption flux of reactive gas particles on the target surface, $\Gamma^{\mathrm{t}}_{\mathrm{exp}}(t)$ is the transfer flux of reactive gas atoms from the target bulk layer into the target surface layer due to the exposure of the compound from the bulk layer caused by sputtering of the surface layer, $\Gamma^{\mathrm{t}}_{\mathrm{disr}}(t)$ is the direct implantation flux of reactive gas ions into the target surface layer, $\Gamma^{\mathrm{t}}_{\mathrm{spr}}(t)$ is the sputtering flux of reactive gas atoms from the target surface layer and $\Gamma^{\mathrm{t}}_{\mathrm{kir}}(t)$ is the knock-on implantation flux of reactive gas atoms from the target surface layer into the target bulk layer.

For the target bulk layer, we use the equation

$$n_0 h_{\mathrm{tb}} x \frac{\mathrm{d}\Theta_{\mathrm{tb}}(t)}{\mathrm{d}t} = \Gamma^{\mathrm{t}}_{\mathrm{dibr}}(t) + \Gamma^{\mathrm{t}}_{\mathrm{kir}}(t) - \Gamma^{\mathrm{t}}_{\mathrm{exp}}(t) - \Gamma^{\mathrm{t}}_{\mathrm{dibm}}(t) \,, \qquad (2)$$

where $\Gamma^{\mathrm{t}}_{\mathrm{dibr}}(t)$ and $\Gamma^{\mathrm{t}}_{\mathrm{dibm}}(t)$ are the direct implantation fluxes of reactive gas ions and metal ions into the target bulk layer, respectively, and the $\Gamma^{\mathrm{t}}_{\mathrm{kir}}(t)$ and $\Gamma^{\mathrm{t}}_{\mathrm{exp}}(t)$ fluxes are the same as those appearing with the opposite sign on the right-hand side of equation (1).

In the following paragraphs, the expressions for the individual fluxes appearing in equations (1) and (2) are given and explained. For simplicity, the time dependence of the fluxes is not explicitly denoted in these expressions. The reader should bear in mind that all parameters used in the following formulae are in general time dependent.

2.2.1.1. Chemisorption of reactive gas particles To account for the specific features of HiPIMS discharges, namely, gas rarefaction and ionization in front of the sputtered target and high degree of dissociation of reactive gas molecules in the flux onto the target, and for a possible increase in the density of the reactive gas in

front of the target due to the reactive gas inlets, we used a generalized formula for the chemisorption flux $\Gamma^{\rm t}_{\rm ch}(t)$, increasing $\Theta_{\rm ts}(t)$,

$$\Gamma^{\rm t}_{\rm ch} = 2R_{\rm t}F_{\rm t}\Gamma_{\rm rm}\alpha^{\rm t}_{\rm ra}D_{\rm t}(1-\Theta_{\rm ts}) + 2R_{\rm t}F_{\rm t}\Gamma_{\rm rm}\alpha^{\rm t}_{\rm rm}(1-D_{\rm t})(1-\Theta_{\rm ts})^2\,. \quad (3)$$

The expression consists of two terms accounting for the chemisorption of reactive gas atoms and molecules on the metal fraction $1-\Theta_{\rm ts}$ of the target surface, respectively. Note that the chemisorption of diatomic reactive gas molecules is described as a dissociative process requiring the presence of two empty surface sites, which is expressed as a term proportional to $(1-\Theta_{\rm ts})^2$, see [39, 40]. The isotropic thermal flux of reactive gas molecules $\Gamma_{\rm rm}$ is related to the reactive gas partial pressure $p_{\rm rm}$, which is measured, as usual, at the wall of the vacuum chamber. The probability of dissociation of reactive gas molecules in the flux onto the target, $D_{\rm t}$, with $0 \le D_{\rm t} \le 1$, defines the factors $2D_{\rm t}$ and $1-D_{\rm t}$ determining the respective fluxes of reactive gas atoms and molecules onto the target. The sticking coefficients of the reactive gas atoms and molecules on the metal fraction of the target surface are denoted as $\alpha^{\rm t}_{\rm ra}$ and $\alpha^{\rm t}_{\rm rm}$, respectively. The reduction factor $R_{\rm t}$, with $0 < R_{\rm t} \le 1$, accounts for a gas rarefaction due to the sputtering wind and for a strong ionization of neutral gas particles in front of the sputtered target during a pulse-on time of HiPIMS discharges (discussed in detail in [3, 41–44]).

Note that the ionized reactive gas particles directed to the target are included in the total ion flux onto the target $\Gamma_{\rm it}$, discussed later, and that we assume the same $R_{\rm t}(t)$ for all neutral gas particles (reactive gas atoms and molecules, inert gas atoms). The overfilling factor of the reactive gas on the target side of the reactive gas inlets, $F_{\rm t}$, with $F_{\rm t} \ge 1$, is used to take into account an increase in the reactive gas flux onto the target due to a local increase in the density of the reactive gas when the reactive gas inlets are placed above the target erosion area and oriented toward the target [21]. Assuming the reactive gas as an ideal gas in thermal equilibrium, the flux $\Gamma_{\rm rm}$ can be calculated [45] as

$$\Gamma_{\rm rm} = \frac{p_{\rm rm}}{\sqrt{2\pi m_{\rm rm} k T_{\rm g}}}\,, \quad (4)$$

where $m_{\rm rm}$ is the mass of the reactive gas molecule, k is the Boltzmann constant and $T_{\rm g}$ is the gas temperature.

Here, it should be mentioned that for $R_{\rm t} = 1$, $D_{\rm t} = 0$ and $F_{\rm t} = 1$, formula (3) becomes $\Gamma^{\rm t}_{\rm ch} = 2\Gamma_{\rm rm}\alpha^{\rm t}_{\rm rm}(1-\Theta_{\rm ts})^2$, used in the surface science literature [39, 40], which is close to $\Gamma^{\rm t}_{\rm ch} = 2\Gamma_{\rm rm}\alpha^{\rm t}_{\rm rm}(1-\Theta_{\rm ts})$, usually used in the models for reactive magnetron sputtering [27].

2.2.1.2. Exposure of compound The transfer flux due to exposure $\Gamma^{\rm t}_{\rm exp}(t)$, increasing $\Theta_{\rm ts}(t)$ and decreasing $\Theta_{\rm tb}(t)$, is expressed [27, 28] as

$$\Gamma^{\rm t}_{\rm exp} = \Gamma_{\rm it}[Y_{\rm mm}(1-\Theta_{\rm ts}) + Y_{\rm mc}\Theta_{\rm ts}]\Theta_{\rm tb}x\,, \quad (5)$$

where $Y_{\rm mm}$ and $Y_{\rm mc}$ are the sputtering yields of metal atoms from the non-reacted metal surface and from the stoichiometric compound MR_x, respectively. Here,

we assume the same sputtering yields for all incident ions, including the ionized sputtered metal atoms directed back to the target.

The ion flux $\Gamma_{\rm it}(t)$ is calculated as

$$\Gamma_{\rm it} = \frac{J_{\rm t} A_{\rm t}}{e A_{\rm te}(1+\gamma)} \,, \tag{6}$$

where e is the elementary charge and $J_{\rm t}(t) = I_{\rm d}(t)/A_{\rm t}$ is the target current density averaged over the total target area $A_{\rm t}$, as usually done to compare results achieved using different magnetron sputter systems.

2.2.1.3. Implantation of particles The direct implantation flux $\Gamma^{\rm t}_{\rm disr}(t)$, increasing $\Theta_{\rm ts}(t)$, can be written in the form

$$\Gamma^{\rm t}_{\rm disr} = \frac{2}{1+D_{\rm t}} \Gamma_{\rm it} f_{\rm r}(1-R_{\rm efr})\Theta_{\rm tb}(1-\Theta_{\rm ts}) \,, \tag{7}$$

where f_r is the fraction of reactive gas (atomic and molecular) ions in the ion flux $\Gamma_{\rm it}$ and $R_{\rm efr}$ is the effective backscattering (reflection) probability of reactive gas atoms from the target after its bombardment by the reactive gas ions with the kinetic energy of $eU_{\rm d}$. The formula (7) describes the direct implantation of those reactive gas atoms into the target surface layer that were not backscattered from the target and cannot be implanted, as assumed, into the stoichiometric compound fraction $\Theta_{\rm tb}$ in the target bulk layer. Note that the reactive gas atoms can reach the target surface layer also by diffusion from the target bulk layer into which they were implanted, but where they did not react with metal atoms. The factor $2/(1+D_{\rm t})$ in equation (7) is a consequence of the realistic assumption that the reactive gas molecules are dissociated with the probability $D_{\rm t}$ before ionization in the discharge plasma (see, for example, the data for oxygen in [40]): The non-dissociated molecular ions with a fraction $(1-D_{\rm t})/(1+D_{\rm t})$ are split into two atoms of half energy $(eU_{\rm d}/2)$ when striking the target surface [28, 29], giving, together with the atomic ions with a fraction $2D_{\rm t}/(1+D_{\rm t})$, the total factor $2(1-D_{\rm t})/(1+D_{\rm t})+2D_{\rm t}/(1+D_{\rm t}) = 2/(1+D_{\rm t})$.

The fraction of the reactive gas atoms, which were not backscattered from the target $1-R_{\rm efr}$, appearing in equation (7), is calculated as

$$1 - R_{\rm efr} = (1-R_{\rm rm})(1-\Theta_{\rm tb}) + (1-R_{\rm rc})\Theta_{\rm tb} \,, \tag{8}$$

where $R_{\rm rm}$ and $R_{\rm rc}$ are the backscattering probabilities of the reactive gas atoms from the non-reacted metal target bulk layer and from the stoichiometric compound in the target bulk layer, respectively. The averaged $R_{\rm efr}$ fraction is used in formula (7) to take into account an inhomogeneous structure of actual target subsurface layers with irregular appearance of non-reacted metal and compound parts in horizontal and vertical directions [29].

Assuming the same ionization probability [27, 29] and rarefaction in front of the target for the inert gas atoms and for the atoms and molecules of a partially

dissociated reactive gas with the partial pressure $p_{\rm rm}$, the fraction $f_{\rm r}$ in equation (7) can be written as

$$f_{\rm r} = (1 - m_{\rm t})\frac{F_{\rm t}p_{\rm rm}}{F_{\rm t}p_{\rm rm} + p_{\rm i}}\,, \tag{9}$$

where $m_{\rm t}$ is the fraction of ionized sputtered metal atoms in the ion flux $\Gamma_{\rm it}$ given by the formula

$$m_{\rm t} = [Y_{\rm mm}(1 - \Theta_{\rm ts}) + Y_{\rm mc}\Theta_{\rm ts}]B_{\rm m}\,. \tag{10}$$

Here, $B_{\rm m}$ is the probability of ionization and subsequent return of sputtered metal atoms onto the target ($0 \leq B_{\rm m} \leq 1$). Assuming the same sputtering yields for all ions incident on the target, including the ionized sputtered metal atoms directed back to the target, we can use equation (6) from [34] in the form $m_{\rm t} = S_{\rm m}\beta_{\rm m}\sigma_{\rm m}$, where $S_{\rm m}$ is the sputtering yield of the target (metal) material, $\beta_{\rm m}$ is the probability of ionization of sputtered metal atoms in front of the target and $\sigma_{\rm m}$ is the probability of return of ionized sputtered metal atoms onto the target. Taking into account that metal atoms are sputtered not only from the non-reacted metal surface ($Y_{\rm mm}$) but also from the stoichiometric compound ($Y_{\rm mc}$) in the case of reactive sputtering and that $B_{\rm m} = \beta_{\rm m}\sigma_{\rm m}$, we can obtain the formula (10).

The knock-on implantation flux $\Gamma^{\rm t}_{\rm kir}(t)$, decreasing $\Theta_{\rm ts}(t)$ and increasing $\Theta_{\rm tb}(t)$, is calculated [27, 28] as

$$\Gamma^{\rm t}_{\rm kir} = \Gamma_{\rm it}Y'_{\rm rc}\Theta_{\rm ts}(1 - \Theta_{\rm tb})\,, \tag{11}$$

where $Y'_{\rm rc}$ is the knock-on implantation yield.

The direct implantation flux $\Gamma^{\rm t}_{\rm dibr}(t)$, increasing $\Theta_{\rm tb}(t)$, is expressed as

$$\Gamma^{\rm t}_{\rm dibr} = \frac{2}{1 + D_{\rm t}}\Gamma_{\rm it}f_{\rm r}(1 - R_{\rm efr})(1 - \Theta_{\rm tb})\,. \tag{12}$$

This expression has a similar form as the aforementioned term $\Gamma^{\rm t}_{\rm disr}(t)$ given by equation (7).

The direct implantation flux $\Gamma^{\rm t}_{\rm dibm}(t)$, decreasing $\Theta_{\rm tb}(t)$, can be written in the form

$$\Gamma^{\rm t}_{\rm dibm} = \Gamma_{\rm it}m_{\rm t}(1 - R_{\rm efm})\Theta_{\rm tb}x\,, \tag{13}$$

where the $m_{\rm t}$ fraction is given by equation (10) and the fraction of the metal atoms that were not backscattered from the target, $1 - R_{\rm efm}$, after its bombardment by the metal ions with the kinetic energy of $eU_{\rm d}$ is calculated as

$$1 - R_{\rm efm} = (1 - R_{\rm mm})(1 - \Theta_{\rm tb}) + (1 - R_{\rm mc})\Theta_{\rm tb}\,, \tag{14}$$

where $R_{\rm mm}$ and $R_{\rm mc}$ are the backscattering probabilities of the metal atoms from the non-reacted metal target bulk layer and from the stoichiometric compound in the target bulk layer, respectively (see similar equation (8)). Formula (13) is derived under the assumption that some metal and reactive gas atoms are displaced out of the target bulk layer by incident metal ions. It should be mentioned that the term $\Gamma^{\rm t}_{\rm dibm}(t)$ describing the direct implantation of metal ions into the target bulk layer

was included in equation (2) as the backward flux of the ionized sputtered metal atoms can significantly affect the composition of the compound layer at the target in reactive HiPIMS.

2.2.1.4. Sputtering of reactive gas atoms The sputtering flux $\Gamma^{\mathrm{t}}_{\mathrm{spr}}(t)$, decreasing $\Theta_{\mathrm{ts}}(t)$, is expressed [27, 28] as

$$\Gamma^{\mathrm{t}}_{\mathrm{spr}} = \Gamma_{\mathrm{it}} Y_{\mathrm{rc}} \Theta_{\mathrm{ts}} \,, \tag{15}$$

where Y_{rc} is the sputtering yield of reactive gas atoms from the stoichiometric compound MR_x. Again, we assume the same sputtering yield for all incident ions.

2.2.2. Substrate surface layer

The composition of the film deposited onto a planar substrate with the area A_{s} is modelled by the composition of the substrate surface layer with a thickness $h_{\mathrm{s}} = h_{\mathrm{ts}}$ of one monolayer [27]. The compound fraction in the target surface layer, Θ_{s}, is given by equation

$$n_0 h_{\mathrm{s}} x \frac{\mathrm{d}\Theta_{\mathrm{s}}(t)}{\mathrm{d}t} = \Gamma^{\mathrm{s}}_{\mathrm{ch}}(t) + \Gamma^{\mathrm{s}}_{\mathrm{der}}(t) - \Gamma^{\mathrm{s}}_{\mathrm{dem}}(t) \,, \tag{16}$$

where $\Gamma^{\mathrm{s}}_{\mathrm{ch}}(t)$ is the chemisorption flux of reactive gas particles on the substrate surface, and $\Gamma^{\mathrm{s}}_{\mathrm{der}}(t)$ and $\Gamma^{\mathrm{s}}_{\mathrm{dem}}(t)$ are the deposition fluxes of reactive gas atoms and metal atoms sputtered from the target, respectively.

2.2.2.1. Chemisorption of reactive gas particles The chemisorption flux $\Gamma^{\mathrm{s}}_{\mathrm{ch}}(t)$, increasing $\Theta_{\mathrm{s}}(t)$, is given by the formula

$$\Gamma^{\mathrm{s}}_{\mathrm{ch}} = 2F_{\mathrm{s}}\Gamma_{\mathrm{rm}}\alpha^{\mathrm{s}}_{\mathrm{ra}} D_{\mathrm{s}}(1-\Theta_{\mathrm{s}}) + 2F_{\mathrm{s}}\Gamma_{\mathrm{rm}}\alpha^{\mathrm{s}}_{\mathrm{rm}}(1-D_{\mathrm{s}})(1-\Theta_{\mathrm{s}})^2 \,. \tag{17}$$

This expression has a similar form as the aforementioned term $\Gamma^{\mathrm{t}}_{\mathrm{ch}}(t)$ given by equation (3). Here, F_{s} is the overfilling factor of the reactive gas on the substrate side of the reactive gas inlets ($F_{\mathrm{s}} \geq 1$) taking into account an increase in the reactive gas flux onto the substrate due to a local increase in the density of the reactive gas particularly when the reactive gas inlets are placed above the target erosion area and oriented toward the substrate [21], D_{s} is the probability of dissociation of reactive gas molecules in the flux onto the substrate ($0 \leq D_{\mathrm{s}} \leq 1$), and $\alpha^{\mathrm{s}}_{\mathrm{ra}}$ and $\alpha^{\mathrm{s}}_{\mathrm{rm}}$ are the sticking coefficients of the reactive gas atoms and molecules on the metal fraction of the substrate surface, respectively.

2.2.2.2. Deposition of particles The deposition flux $\Gamma^{\mathrm{s}}_{\mathrm{der}}(t)$, increasing $\Theta_{\mathrm{s}}(t)$, is calculated as

$$\Gamma^{\mathrm{s}}_{\mathrm{der}} = \Gamma_{\mathrm{it}} Y_{\mathrm{rc}} \Theta_{\mathrm{ts}} (1-B_{\mathrm{r}}) f_{\mathrm{trr}} \frac{A_{\mathrm{te}}}{A_{\mathrm{s}}} \alpha^{\mathrm{s}}_{\mathrm{ra}} (1-\Theta_{\mathrm{s}}) \,, \tag{18}$$

where B_{r} is the probability of ionization and subsequent return of sputtered reactive gas atoms onto the target ($0 \leq B_{\mathrm{r}} \leq 1$) and f_{trr} is the transport factor determining

the fraction of the reactive gas atoms sputtered from the target erosion area $A_{\rm te}$ and not directed back to the target if ionized (factor $1 - B_{\rm r}$) that strike the substrate area $A_{\rm s}$ as neutral atoms or ions. The $f_{\rm trr}$ factor accounts for a collisional scattering of the sputtered atoms and their ions during transfer to the substrate. Let us recall that losses of the sputtered atoms to chamber walls are affected by a target erosion profile defining the initial emission angles of the sputtered particles [29] and that the losses of ionized sputtered atoms during the transfer to substrate are usually higher than those of the sputtered neutrals in HiPIMS discharges [1–3].

The deposition flux $\Gamma^{\rm s}_{\rm dem}(t)$, decreasing $\Theta_{\rm s}(t)$, is expressed as

$$\Gamma^{\rm s}_{\rm dem} = \Gamma_{\rm it}[Y_{\rm mm}(1 - \Theta_{\rm ts}) + Y_{\rm mc}\Theta_{\rm ts}](1 - B_{\rm m}) f_{\rm trm}\frac{A_{\rm te}}{A_{\rm s}}\Theta_{\rm s} x\,, \qquad (19)$$

where $f_{\rm trm}$ is the transport factor determining the fraction of the metal atoms sputtered from the target erosion area $A_{\rm te}$ and not directed back to the target if ionized (factor $1 - B_{\rm m}$) that strike the substrate area $A_{\rm s}$ as neutral atoms or ions. It should be noted that the transport factors $f_{\rm trr}$ and $f_{\rm trm}$, appearing in equations (18) and (19), respectively, are not usually used in model equations for reactive magnetron sputtering where $A_{\rm s}$ includes not only the substrate area, as in our case, but also the area of chamber walls [26, 27] with generally different deposition rates of films [23, 29].

2.3. Input parameters and solution procedure

Input parameters of the model can be divided into three groups, namely, process parameters, internal discharge parameters and material parameters.

The process parameters include the discharge characteristics ($U_{\rm d}$ and $I_{\rm d}$), the partial pressures of gases ($p_{\rm i}$ and $p_{\rm rm}$), and the geometrical characteristics of a planar magnetron target ($A_{\rm t}$ and $A_{\rm te}$) and a planar substrate ($A_{\rm s}$).

The internal discharge parameters are the reduction factor of the flux of reactive gas atoms and molecules onto the target ($R_{\rm t}$), the dissociation probabilities of reactive gas molecules ($D_{\rm t}$ and $D_{\rm s}$), the probabilities of ionization and subsequent return of sputtered atoms onto the target ($B_{\rm m}$ and $B_{\rm r}$), the transport factors of sputtered atoms ($f_{\rm trm}$ and $f_{\rm trr}$), the overfilling factors of the reactive gas ($F_{\rm t}$ and $F_{\rm s}$), and the gas temperature $T_{\rm g}$. Let use recall that all these parameters are in general time dependent.

The material parameters include the atomic density of the target material before reaction (n_0), the stoichiometry factor (x) of the compound, the mass of the reactive gas molecule ($m_{\rm rm}$), the thicknesses of the compound layers ($h_{\rm ts} = h_{\rm s}$ and $h_{\rm tb}$), the sputtering yields ($Y_{\rm mm}$, $Y_{\rm mc}$ and $Y_{\rm rc}$) and the knock-on implantation yield ($Y'_{\rm rc}$) of atoms, the effective ion-induced secondary electron emission yield (γ), the backscattering probabilities of the reactive gas atoms ($R_{\rm rm}$ and $R_{\rm rc}$) and the metal atoms ($R_{\rm mm}$ and $R_{\rm mc}$) from the target, and the sticking coefficients of the reactive gas particles on the target ($\alpha^{\rm t}_{\rm ra}$ and $\alpha^{\rm t}_{\rm rm}$) and the substrate ($\alpha^{\rm s}_{\rm ra}$ and $\alpha^{\rm s}_{\rm rm}$).

The atomic density of the target material can be calculated as

$$n_0 = \frac{\rho N_\mathrm{A}}{M_\mathrm{m}}\,, \tag{20}$$

where N_A is the Avogadro constant, ρ is the mass density and M_m is the molar mass of the target material. Assuming the target material homogeneous and isotropic, we can estimate [29] its average monolayer thickness as $h_\mathrm{ts} = n_0^{-1/3}$.

As mentioned above, the sputtering yields Y_mm, Y_mc and Y_rc are assumed to be independent of the type of incident ions [27, 28], which is a reasonable assumption taking into account that the gas ion flux onto the target is typically dominated by inert gas ions and that the sputtering yields for the incident ionized sputtered metal atoms are not too different from those for the incident inert gas ions [34]. The sputtering yields are considered to be dependent on the kinetic energy of incident ions $\varepsilon = eU_\mathrm{d}$.

With these inputs, the model equations (1), (2) and (16) are solved in the Matlab environment using the well-known Runge-Kutta method. The initial compound fractions $\Theta_\mathrm{ts}(t)$, $\Theta_\mathrm{tb}(t)$ and $\Theta_\mathrm{s}(t)$ are set to zero and the equations are numerically integrated over the consecutive pulse periods, T_p, of the power supply. The integration is stopped when the difference in all compound fractions between the beginning and the end of the same period becomes lower than the tolerance, δ, which can be written as

$$\max_{i=\mathrm{ts,tb,s}} |\Theta_i(T_\mathrm{p}) - \Theta_i(0)| < \delta\,. \tag{21}$$

Then, the functions $\Theta_\mathrm{ts}(t)$, $\Theta_\mathrm{tb}(t)$ and $\Theta_\mathrm{s}(t)$ are identical in the subsequent pulse periods and the sputtering process is considered stable. In our calculations, we used $\delta = 2 \times 10^{-4}$ which gives a good balance between accuracy and computational time.

For the stabilized state, we calculate the time-dependent fluxes $\Gamma_\mathrm{pr}(t)$ for the individual processes, which determine the compound fractions $\Theta_\mathrm{ts}(t)$, $\Theta_\mathrm{tb}(t)$ and $\Theta_\mathrm{s}(t)$ given by equations (1), (2) and (16). To evaluate the fractions of the individual processes that contribute to the increase or decrease of the content of reactive gas atoms in the corresponding target and substrate layers during a whole film deposition after stabilization of the sputtering process, the integral quantity I_pr (in particles per cm^2 per pulse period T_p) is introduced as

$$I_\mathrm{pr} = \int_0^{T_\mathrm{p}} \Gamma_\mathrm{pr}(t)\mathrm{d}t\,. \tag{22}$$

Here, it should be mentioned that the deposition of films is a periodic process and that $\Gamma_\mathrm{pr}(t) = 0$ for $t_\mathrm{on} < t \leq T_\mathrm{p}$, where t_on is the pulse duration, excepting the chemisorption fluxes $\Gamma^\mathrm{t}_\mathrm{ch}(t)$ and $\Gamma^\mathrm{s}_\mathrm{ch}(t)$ defined by equations (3) and (17), respectively.

For the chemisorption processes, we use

$$I_\mathrm{ch,on} = \int_0^{t_\mathrm{on}} \Gamma_\mathrm{ch}(t)\mathrm{d}t \tag{23}$$

and

$$I_{\mathrm{ch,off}} = \int_{t_{\mathrm{on}}}^{T_{\mathrm{p}}} \Gamma_{\mathrm{ch}}(t)\mathrm{d}t\,, \tag{24}$$

where $I_{\mathrm{ch,on}}$ and $I_{\mathrm{ch,off}}$ account for the chemisorption of reactive gas particles during the pulse-on time and the pulse-off time, respectively.

The deposition rate of metal atoms on the substrate area A_{s} (in particles per second) after stabilization of the sputtering process is expressed (see equation (19)) as

$$M_{\mathrm{s}} = \frac{1}{T_{\mathrm{p}}} \int_{0}^{T_{\mathrm{p}}} \Gamma_{\mathrm{it}}[Y_{\mathrm{mm}}(1-\Theta_{\mathrm{ts}}) + Y_{\mathrm{mc}}\Theta_{\mathrm{ts}}](1-B_{\mathrm{m}}) f_{\mathrm{trm}} A_{\mathrm{te}}\mathrm{d}t\,. \tag{25}$$

Then, the deposition rate of films (in nm per second), a_{D}, can be written as

$$a_{\mathrm{D}} = \frac{M_{\mathrm{s}}}{n_{\mathrm{m,c}} A_{\mathrm{s}}}\,, \tag{26}$$

where $n_{\mathrm{m,c}}$ is the atomic density of the metal atoms in the deposited compound. Thus, we are able to compare the deposition rate calculated by the model with experimental data.

The parametric model developed allows us to investigate reactive HiPIMS processes under various discharge conditions. The calculated time-dependent compound fractions $\Theta_{\mathrm{ts}}(t)$, $\Theta_{\mathrm{tb}}(t)$ and $\Theta_{\mathrm{s}}(t)$, together with the corresponding fluxes for the individual processes $\Gamma_{\mathrm{pr}}(t)$ increasing or decreasing the content of reactive gas atoms in the target and substrate layers, are of key importance for understanding the complicated dynamics of the processes on the target and substrate surfaces during high-power pulses and in pulse-off times. The integral quantities I_{pr} (equation (22)) and M_{s} (equation (25)) can be used to evaluate the important characteristics of the deposition processes, namely, the fractions of the individual processes changing the content of reactive gas atoms in the target and substrate layers during a whole film deposition, and the deposition rate of films, respectively.

3. Application of the model to reactive high-power impulse magnetron sputtering of ZrO_2 films

We simulate the sputtering of zirconium in a mixture of argon and oxygen. The stoichiometric compound forming on the target and substrate is zirconium dioxide, ZrO_2. A basis for the application of the presented model is a recent experimental work carried out in our laboratories, where, however, a pulsed (i.e., not continuous) reactive gas (oxygen) flow control was used for high-rate reactive HiPIMS depositions of densified stoichiometric ZrO_2 films [21]. The elemental composition (in at %) of the films was characterized as $Zr_{32-34}O_{65-67}$ with low contamination level (H content less than 1 at %). The main aim of the present study is to consistently explain large differencies between the deposition rates of the ZrO_2 films achieved for two different configurations (different locations and opposite orientations) of the

O_2 inlets, placed in front of the sputtered target, under similar discharge conditions (table 2). Moreover, model calculations were carried out to explain the effects of the increased target power densities (up to 2.3 kWcm^{-2}) applied during shortened voltage pulses (from 200 μs to 50 μs), and to investigate the effects of the gas rarefaction and ionization in front of the sputtered target, the backward flux of the ionized sputtered atoms onto the target and the dissociation of reactive gas molecules on the processes on the target and substrate surfaces during the reactive HiPIMS depositions, and on the deposition rates of the ZrO_2 films produced.

3.1. Experimental conditions and results

In the work [21], the ZrO_2 films were deposited using a strongly unbalanced magnetron source with a directly water-cooled planar zirconium target (99.99 % purity, diameter of 100 mm and thickness of 6 mm) in a standard stainless-steel vacuum chamber (diameter of 507 mm and length of 520 mm). The magnetron was driven by a high-power pulsed dc power supply (HMP 2/1, Hüttinger Elektronik). The repetition frequency, f_{rep}, was 500 Hz and the pulse duration, t_{on}, ranged from 50 μs to 200 μs with the corresponding duty cycle $t_{\mathrm{on}}/T_{\mathrm{p}} = 2.5\,\% - 10\,\%$, where the pulse period $T_{\mathrm{p}} = 1/f_{\mathrm{rep}}$.

A reactive gas (oxygen) was admitted into the vacuum chamber from a source via mass flow controllers and two corundum conduits (figure 1). Two O_2 inlets with a diameter of 1 mm were placed symmetrically above the target erosion area at the same distance of 20 mm from the target surface and oriented toward the target (denoted as "to-target O_2 inlet" configuration) or at the same (optimized) distance of 25 mm from the target surface and oriented toward the substrate (denoted as "to-substrate O_2 inlet" configuration).

Prior to the admission of O_2 into the system, the Ar flow rate was set to 30 sccm and the pumping speed of a diffusion pump (backed with a rotary pump) was adjusted to attain the argon partial pressure $p_{\mathrm{i}} = 2$ Pa. The settings of the Ar flow rate and the pumping speed were not changed during the experiments. During the deposition, a process controller used provided a control feed-back signal to the two O_2 mass flow controllers to adjust the pulsed O_2 flow rate into the vacuum chamber ($\Phi_{\mathrm{ox}}(t)$ = const or 0) by adjusting the duration of the O_2 flow rate pulses. Typical durations of the Φ_{ox} pulses and of the corresponding Φ_{ox} pulse-off times were in the range of $2-3$ seconds and $2-5$ seconds, respectively. A detailed description of the pulsed O_2 flow control is given in [21]. The oxygen partial pressure, p_{rm}, measured at a point on the chamber wall of 270 mm from the target–substrate axis (figure 1), oscillated between 0 and 0.08 Pa during the depositions. The values of p_{i} and of $p_{\mathrm{i}} + p_{\mathrm{rm}}$ were measured using a high-stability capacitance manometer (Baratron, type 627, MKS Instruments) with the accuracy of approximately 1 % [21].

Waveforms of the magnetron voltage, $U_{\mathrm{d}}(t)$, and the discharge current, $I_{\mathrm{d}}(t)$,

were monitored (figure 2) and the average target power density in a discharge pulse, S_{da}, was evaluated using the formula

$$S_{\mathrm{da}} = \frac{1}{t_{\mathrm{on}}} \int_0^{t_{\mathrm{on}}} U_{\mathrm{d}}(t) J_{\mathrm{t}}(t) \mathrm{d}t\,. \tag{27}$$

Here, the target current density $J_{\mathrm{t}}(t) = I_{\mathrm{d}}(t)/A_{\mathrm{t}}$, where A_{t} is the total area of the target (78.54 cm^2 in our case). Note that S_{da} is time dependent during a deposition as the discharge pulses are realized at time-varying p_{rm} on the scale of seconds (see figure 2 and table 2). An analogous integral expression was used to calculate the average magnetron voltage in a pulse, U_{da}. The deposition-averaged target power density, $\langle S_{\mathrm{d}} \rangle$, was evaluated using the formula

$$\langle S_{\mathrm{d}} \rangle = \frac{1}{t_{\mathrm{e}} - t_{\mathrm{s}}} \int_{t_{\mathrm{s}}}^{t_{\mathrm{e}}} U_{\mathrm{d}}(t) J_{\mathrm{t}}(t) \mathrm{d}t\,, \tag{28}$$

where t_{s} and t_{e} are the start and end times of the deposition.

The deposition rate of the $\mathrm{ZrO_2}$ films, a_{D}, achieved for the target-to-substrate distance $d = 100$ mm and the time-averaged fractions of the $\mathrm{O^+}$ and $\mathrm{O_2^+}$ ions in the total flux of positive ions onto the substrate $\Gamma(\mathrm{O^+})$ and $\Gamma(\mathrm{O_2^+})$, respectively, are given in table 2 together with the corresponding discharge characteristics t_{on}, $\langle S_{\mathrm{d}} \rangle$, S_{da} and U_{da}. Here, it should be mentioned that the larger distance of the to-substrate oriented $\mathrm{O_2}$ inlets from the target (25 mm), proposed for the high-rate reactive HiPIMS of the $\mathrm{ZrO_2}$ films at the much higher $\langle S_{\mathrm{d}} \rangle = 50\,\mathrm{Wcm^{-2}}$, proved unsuitable at a low value of $\langle S_{\mathrm{d}} \rangle = 5.4\,\mathrm{Wcm^{-2}}$ [21]. As a consequence, the value of a_{D} was only 5 nm/min. Note that for the to-target $\mathrm{O_2}$ inlet at $\langle S_{\mathrm{d}} \rangle \simeq 50\,\mathrm{Wcm^{-2}}$, the lowest values of S_{da} (at the lowest values of p_{rm}) correspond, somewhat counterintuitively, to the highest values of U_{da} and vice versa. The reason is that the magnetron voltage $U_{\mathrm{d}}(t)$ decreases during a discharge pulse even in the constant-voltage mode of the pulsed power supply (figure 2). Moreover, this decrease is more pronounced for the to-target $\mathrm{O_2}$ inlet at the highest value of p_{rm} due to a bigger increase in $J_{\mathrm{t}}(t)$ during a pulse (see figure 3 in [21]) leading to the lowest value of U_{da} for the highest value of S_{da}.

3.2. Model inputs

In table 3, we present the discharge characteristics and the corresponding basic sets of internal discharge parameters used for various discharge regimes in our model calculations carried out with a fixed argon partial pressure $p_{\mathrm{i}} = 2$ Pa and a fixed oxygen partial pressure p_{rm} ranging from 0.01 to 0.14 Pa (to account for the accuracy of the measurement mentioned) at the pulse period $T_{\mathrm{p}} = 2000\,\mu$s. The total area of the target and the target erosion area were $A_{\mathrm{t}} = 78.54\,\mathrm{cm}^2$ and $A_{\mathrm{te}} = 0.5A_{\mathrm{t}}$, respectively. The substrate area was $A_{\mathrm{s}} = 0.25A_{\mathrm{t}}$ at the target-to-substrate distance $d = 100$ mm, where we assumed a uniform film deposition.

The labels of the discharge regimes are given in the form "$\langle S_{\mathrm{d}} \rangle$-$t_{\mathrm{on}}$-$\mathrm{O_2}$ inlet orientation", where T stands for the to-target $\mathrm{O_2}$ inlet orientation and S stands for

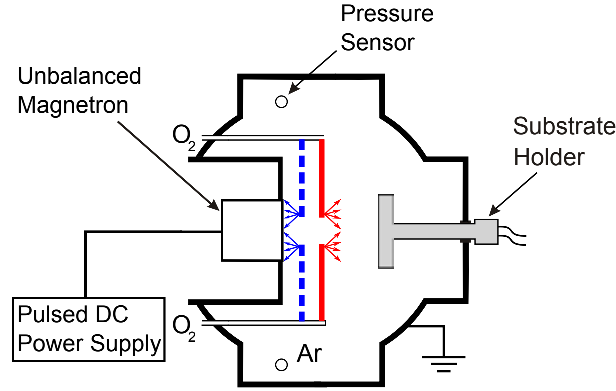

Figure 1. Schematic diagram of the deposition device with two different locations and orientations of the O_2 inlets in front of the target. Dashed lines represent the to-target O_2 inlet configuration (20 mm from the target surface), and solid lines represent the to-substrate O_2 inlet configuration (25 mm from the target surface). Positions of the pressure sensor (270 mm from the target-substrate axis) and the Ar inlet in the back side of the vacuum chamber are also shown. Adapted from [21].

Table 2. Deposition characteristics of the stoichiometric ZrO_2 films for the to-target O_2 inlet (denoted as T) and the to-substrate O_2 inlet (denoted as S) at the preset deposition-averaged target power densities $\langle S_{\rm d}\rangle$ = 5.2, 5.4 and $51 - 53\,{\rm Wcm^{-2}}$, pulse durations $t_{\rm on} = 200\,\mu$s and $50\,\mu$s, and a fixed argon partial pressure $p_{\rm i} = 2\,$Pa. The oxygen partial pressures, $p_{\rm rm}$, oscillated between 0 and 0.08 Pa. Here, $S_{\rm da}$ is the average target power density in a pulse, $U_{\rm da}$ is the corresponding average magnetron voltage in a pulse, $a_{\rm D}$ is the deposition rate of films, and $\Gamma(O^+)$ and $\Gamma(O_2^+)$ are the fractions of the O^+ and O_2^+ ions, respectively, in the total flux of positive ions onto the substrate. Adapted from [21].

Inlet	$t_{\rm on}$ (μs)	$\langle S_{\rm d}\rangle$ ($\rm Wcm^{-2}$)	$S_{\rm da}$ ($\rm Wcm^{-2}$)	$U_{\rm da}$ (V)	$a_{\rm D}$ (nm/min)	$\Gamma(O^+)$ (%)	$\Gamma(O_2^+)$ (%)
T	200	5.2	44 – 51	403 – 408	11	0.5	1.7
S	200	5.4	35 – 58	351 – 347	5	0.5	2.3
T	200	51.0	350 – 770	516 – 453	62	0.4	0.5
S	200	52.0	370 – 540	484 – 513	118	1.7	2.8
T	50	53.0	1650 – 2270	619 – 576	15	3.2	0.7
S	50	53.0	1700 – 2100	673 – 679	80	3.8	0.1

the to-substrate O_2 inlet orientation. The 5-cont regime represents a conventional continuous dc reactive magnetron sputtering with a standard O_2 inlet at a target power density of $5\,{\rm Wcm^{-2}}$ used for comparison in this work.

The target current densities $J_{\rm t}(t)$, relating to the discharge regimes considered, are derived from the measured waveforms (figure 2) using a piecewise linear function approximation and the corresponding constant values of $U_{\rm da}$ and $S_{\rm da}$ given in table 3. Let us emphasize that the durations of the initial rise in $J_{\rm t}(t)$, $t_{\rm in}$, presented in table 3, are in good agreement with our experimental data (shown only for the

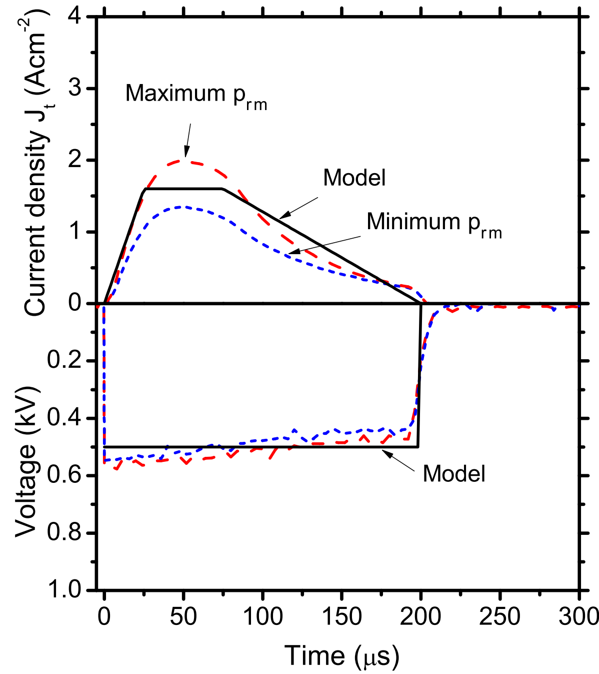

Figure 2. Waveforms of the magnetron voltage, U_{d}, and the target current density, J_{t}, for a preset deposition-averaged target power density $\langle S_{\mathrm{d}} \rangle = 52\,\mathrm{Wcm}^{-2}$ at a pulse duration $t_{\mathrm{on}} = 200\,\mu\mathrm{s}$ and the to-substrate O_2 inlet. During the experiment, the waveforms oscillate between the "Maximum p_{rm}" and "Minimum p_{rm}" curves, as the oxygen inflow varies to control the reactive sputter deposition of stoichiometric ZrO_2 films. The approximate average waveforms used in the model are shown by solid lines.

50-200-S regime in figure 2).

Owing to the lack of data in the literature, the time evolution of the reduction factor $R_{\mathrm{t}}(t)$ and the probability $B_{\mathrm{m}}(t)$ during pulses, and the values of $R_{\mathrm{t}}(t_{\mathrm{in}})$ and $B_{\mathrm{m}}(t_{\mathrm{in}})$ were estimated on the basis of the data obtained for HiPIMS of metals. We used the data from [42, 43] for determination of R_{t}, and from [43, 46–48] for determination of B_{m}. With a Cu target, R_{t} decreased to 0.58 during a pulse at $S_{\mathrm{da}} = 500\,\mathrm{Wcm}^{-2}$ [42]. With an Al target, R_{t} decreased to 0.50 during a pulse at $S_{\mathrm{da}} \lesssim 500\,\mathrm{Wcm}^{-2}$ [43]. We used $R_{\mathrm{t}}(t_{\mathrm{in}}) = 0.5$ for $S_{\mathrm{da}} = 500\,\mathrm{Wcm}^{-2}$ (see table 3). Taking into account that R_{t} decreases with an increasing S_{da}, we used extrapolated values $R_{\mathrm{t}}(t_{\mathrm{in}}) = 0.9$ for $S_{\mathrm{da}} = 50\,\mathrm{Wcm}^{-2}$ and $R_{\mathrm{t}}(t_{\mathrm{in}}) = 0.2$ for $S_{\mathrm{da}} = 2000\,\mathrm{Wcm}^{-2}$. With the Al target, B_{m} increased up to 0.6 during a pulse at $S_{\mathrm{da}} \lesssim 500\,\mathrm{Wcm}^{-2}$ [43]. With a Nb target, $B_{\mathrm{m}} = 0.83$ for a strong magnetron's magnetic field and $B_{\mathrm{m}} = 0.46$ for a weak magnetron's magnetic field at $S_{\mathrm{da}} = 2500\,\mathrm{Wcm}^{-2}$ [46]. We used $B_{\mathrm{m}}(t_{\mathrm{in}}) = 0.5$ for $S_{\mathrm{da}} = 500\,\mathrm{Wcm}^{-2}$ (see table 3). Based on the measured difference in the deposition rate per average target power density in a period obtained for $S_{\mathrm{da}} = 35\,\mathrm{Wcm}^{-2}$ and $S_{\mathrm{da}} = 450\,\mathrm{Wcm}^{-2}$ with a Zr target [47], we estimated $B_{\mathrm{m}}(t_{\mathrm{in}}) = 0.2$ for $S_{\mathrm{da}} = 50\,\mathrm{Wcm}^{-2}$ (see table 3). Taking into account that the

ionization probability of sputtered atoms, β_{m}, increases with S_{da} and that the ion return probability, σ_{m}, decreases with an increasing U_{da} [48], we estimated, using a relation $B = \beta_{\mathrm{m}}\sigma_{\mathrm{m}}$, $B_{\mathrm{m}}(t_{\mathrm{in}}) = 0.6$ for $S_{\mathrm{da}} = 2000\,\mathrm{Wcm}^{-2}$ (see table 3). Taking into account a big difference between the ionization energy of zirconium (6.63 eV) and atomic oxygen (the lowest ionization limit of 13.62 eV [49]), we put $B_{\mathrm{m}} = 2B_{\mathrm{r}}$. Under the simplifying assumptions that the probabilities of the dissociation of reactive gas molecules in the flux onto the target and the substrate are the same and that the reactive gas molecules are dissociated with the probabilities $D_{\mathrm{t}} = D_{\mathrm{s}}$ before ionization in the discharge plasma (see equations (7) and (12)), we used the measured fluxes $\Gamma(\mathrm{O}^{+})$ and $\Gamma(\mathrm{O}_2^{+})$, given in table 2, to estimate the values of $D_{\mathrm{t}} = D_{\mathrm{s}}$. The time evolution of the probabilities $D_{\mathrm{t}}(t) = D_{\mathrm{s}}(t)$ during the pulse-off time was determined on the basis of the recent measurements of Britun et al. [50], who reported a relatively slow decrease in the population of oxygen atom metastable states with time after the pulse termination.

The estimations of the overfilling factors F_{t} and F_{s} are based on our own measurements (unpublished), which were similar to those performed by Rossnagel [51]. A second high-stability capacitance manometer was mounted at the end of a movable, 25 mm diameter tube which extended through the chamber wall to the position on the substrate side in front of one of two O_2 inlets (figure 1). The tube was oriented toward the O_2 inlet and the axis of its bent last part was perpendicular to the target surface. The measurements were carried out without a discharge to separate the effect of the local O_2 injection. To eliminate a natural increase of the oxygen partial pressure in the vacuum chamber with time, we evaluated only the pressure oscillations caused by first two Φ_{ox} pulses with a 2 – 3 second duration. We found that a maximum value of the local oxygen partial pressure at a position of 35 mm from the target surface, i.e. 10 mm from the O_2 inlet, was up to 3 times higher for the to-substrate O_2 inlet with the same Φ_{ox} pulses as at $\langle S_{\mathrm{d}}\rangle = 50\,\mathrm{Wcm}^{-2}$ than the corresponding maximum value $p_{\mathrm{rm}} = 0.08$ Pa measured at the wall of the vacuum chamber. The minimum local oxygen partial pressure was at least 0.03 Pa whereas $p_{\mathrm{rm}} = 0$ under these conditions. Estimating the values of F_{t} and F_{s}, we took into account collisions of oxygen atoms and molecules on the way to the target and substrate, respectively, and the fact that the pulsing Φ_{ox} values were typically 1.4 times higher for the to-substrate O_2 inlet [21].

In this work, we used the transport factors $f_{\mathrm{trm}} = f_{\mathrm{trr}} = 0.0081$. The value of f_{trm} was determined on the assumption that the deposition rate $a_{\mathrm{D}} = 118$ nm/min obtained experimentally for the densified stoichiometric ZrO_2 films at the 50-200-S regime (table 2) is equal to that calculated using the present model (equations (25) and (26)) at $p_{\mathrm{rm}} = 0.05$ Pa. It should be mentioned that f_{trm} would be 0.0079 if we identified $a_{\mathrm{D}} = 11$ nm/min obtained experimentally at the 5-200-T regime (table 2) with that calculated using the model at $p_{\mathrm{rm}} = 0.05$ Pa. We assume $T_{\mathrm{g}} = 300$ K in all simulations.

As for the material parameters, the atomic density of the non-reacted Zr target

$n_0 = 4.30 \times 10^{22}\,\mathrm{cm}^{-3}$, the stoichiometry factor of ZrO_2, $x = 2$, and the thickness of the target and substrate surface layers $h_{\mathrm{ts}} = h_{\mathrm{s}} = 2.85\,\text{Å}$. Based on the calculations of the implantation depth of oxygen ions into the Zr target using the SDTrimSP program [37], we evaluated the thickness of the target bulk layer $h_{\mathrm{tb}} = 50\,\text{Å}$. We also used the SDTrimSP program to determine the backscattering probabilities of the oxygen atoms $R_{\mathrm{rm}} = 0.32$ and $R_{\mathrm{rc}} = 0.12$, and of the zirconium atoms $R_{\mathrm{mm}} = 0.02$ and $R_{\mathrm{mc}} = 0.005$ (see details in [21]), as well as the sputtering yields Y_{mm}, Y_{mc} and Y_{rc} (figure 3), and the knock-on implantation yield $Y'_{\mathrm{rc}} = 0.6$. Let us recall that the backscattering probabilities are only weakly dependent on the energy of ions striking the target during pulses. In the range of the Ar^+ ion kinetic energy $\varepsilon = eU_{\mathrm{da}}$ from 200 eV to 1500 eV, the calculated data for the sputtering yields Y_{mm}, Y_{mc} and Y_{rc} can be fitted by the following power-law functions

$$Y_{\mathrm{mm}} = 2.10 \times 10^{-2} \times (\varepsilon - 91.4)^{0.563}\,, \tag{29}$$

$$Y_{\mathrm{mc}} = 1.78 \times 10^{-4} \times (\varepsilon - 162.0)^{0.850}\,, \tag{30}$$

$$Y_{\mathrm{rc}} = 1.43 \times 10^{-2} \times (\varepsilon - 90.7)^{0.538}\,. \tag{31}$$

The effective ion-induced secondary electron emission yield $\gamma = 0.1$ in all calculations.

We assumed the sticking coefficients $\alpha^{\mathrm{t}}_{\mathrm{ra}} = \alpha^{\mathrm{s}}_{\mathrm{ra}} = 1.0$ for O atoms (see, e.g., [25, 27, 28, 39]). For O_2 molecules on the target surface, we used the estimations $\alpha^{\mathrm{t}}_{\mathrm{rm}} = 0.2$ (table 5.1 in chapter 5, p 184 in [52]) during discharge pulses when $t \le t_{\mathrm{on}}$, $\alpha^{\mathrm{t}}_{\mathrm{rm}} = 0.5$ in a short period of the plasma activation $t_{\mathrm{ac}} = 25\,\mu$s after the pulses when $t_{\mathrm{on}} < t \le t_{\mathrm{on}} + t_{\mathrm{ac}}$, in which the electron and ion densities between the target and substrate remain very high [53], and $\alpha^{\mathrm{t}}_{\mathrm{rm}} = 0.005$ [39] in a successive part of the pulse-off times when $t_{\mathrm{on}} + t_{\mathrm{ac}} < t \le T_{\mathrm{p}}$. Here, it should be mentioned that vibrational excitations of the O_2 molecules in a discharge plasma can result in their significantly enlarged sticking coefficients [54]. During the time t_{ac} after the pulse termination, the sticking coefficient $\alpha^{\mathrm{t}}_{\mathrm{rm}}$ is effectively increased by including a relatively high flux of low-energy O_2^+ ions coming from the discharge plasma onto the target. Let us recall that according to the SDTrimSP program [37], the backscattering probability of O atoms from a metal part of the Zr target is 0.41 for the kinetic energy of O_2^+ incident ions of 25 eV. For O_2 molecules on the substrate surface, we used the estimation $\alpha^{\mathrm{s}}_{\mathrm{rm}} = 0.5$ when $t \le t_{\mathrm{on}} + t_{\mathrm{ac}}$. It takes into account particularly the effect of enhanced flux of the low-energy O_2^+ ions onto substrates in reactive HiPIMS discharges, but also a generally higher sticking coefficient of the reactive gas molecules on the substrate surface layer than on the target surface layer [52]. We assumed $\alpha^{\mathrm{s}}_{\mathrm{rm}} = 0.005$ [39] in the remaining part of the pulse period when $t_{\mathrm{on}} + t_{\mathrm{ac}} < t \le T_{\mathrm{p}}$. For the 5-cont regime, we set $\alpha^{\mathrm{t}}_{\mathrm{rm}} = \alpha^{\mathrm{s}}_{\mathrm{rm}} = 0.2$.

3.3. Model calculations and discussion

In the following, we present the results of model calculations. First, we show and explain the time evolution of the compound fractions in the target and substrate

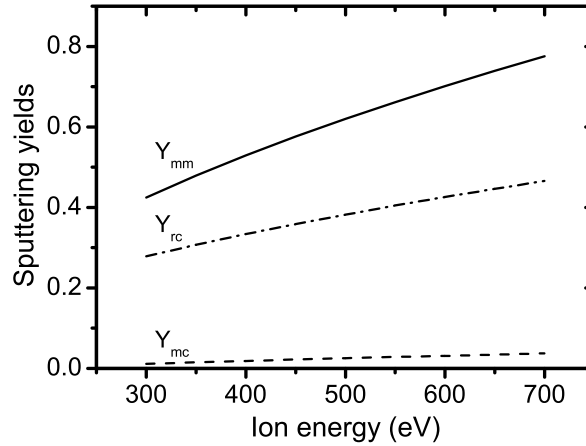

Figure 3. The sputtering yields of Zr atoms from a non-reacted Zr surface, Y_{mm}, and of Zr and O atoms from a ZrO_2 surface, Y_{mc} and Y_{rc}, respectively, as functions of the kinetic energy of incident Ar^+ ions. Calculated by the SDTrimSP program [37].

layers during a pulse period (figures 4 and 5), and the fractions of the individual processes changing the oxygen content in the target and substrate layers during the whole film deposition (tables 4–6) after stabilization of the sputtering process at a fixed oxygen partial pressure $p_{\mathrm{rm}} = 0.05\,\mathrm{Pa}$. This partial pressure is close to the mean value of p_{rm} during the controlled oscillations in experiments. Then, we show and explain the stabilized compound fractions in the target and substrate surface layers obtained for different discharge regimes at various fixed oxygen partial pressures (figures 6–8). Lastly, we present and discuss the deposition rates of films calculated by the model (figure 9).

3.3.1. Compound fractions in the target and substrate layers

3.3.1.1. Fixed oxygen partial pressure $p_{\mathrm{rm}} = 0.05\,\mathrm{Pa}$ Figures 4 and 5 show the stabilized time evolution of the compound fractions in the target and substrate layers during a pulse period $T_{\mathrm{p}} = 2000\,\mu\mathrm{s}$ for the 50-200 regimes and the 50-50 regimes at $p_{\mathrm{rm}} = 0.05\,\mathrm{Pa}$. As can be seen, the changes in Θ_{s}, Θ_{ts} and Θ_{tb} during a pulse period are relatively small. The largest change (from 22 % to 15 %) was observed for the compound fraction Θ_{ts} at the 50-50-T regime. In contrast, almost negligible time changes were observed for the low compound fraction Θ_{tb}, as illustrated for the 50-200-S regime in figure 5. The main reason is a much higher thickness $h_{\mathrm{tb}} = 50\,\mathrm{Å}$ compared with $h_{\mathrm{ts}} = h_{\mathrm{s}} = 2.85\,\mathrm{Å}$.

Very low values of $\Theta_{\mathrm{ts}}(t) \leq 8\,\%$ and $\Theta_{\mathrm{ts}} \leq 12\,\%$ achieved for the pulse durations $t_{\mathrm{on}} = 200\,\mu\mathrm{s}$ and $t_{\mathrm{on}} = 50\,\mu\mathrm{s}$, respectively, with the to-substrate O_2 inlet (figures 4 and 5) can be explained mainly by a high knock-on implantation flux of oxygen atoms $\Gamma^{\mathrm{t}}_{\mathrm{kir}}$ (see equation (11) and the I_{kir} fractions of 61.4 % and 56.8 % in table 4) and by a high sputtering flux of oxygen atoms $\Gamma^{\mathrm{t}}_{\mathrm{spr}}$ (see equation (15) and the I_{spr}

Table 3. Discharge characteristics and the corresponding basic sets of internal discharge parameters used for various discharge regimes in our model calculations. The labels of the discharge regimes are given in the form "$\langle S_\mathrm{d}\rangle$-$t_\mathrm{on}$-$O_2$ inlet orientation", where T stands for the to-target O_2 inlet and S stands for the to-substrate O_2 inlet. The 5-cont regime represents a continuous dc reactive sputtering at a target power density of $5\,\mathrm{Wcm}^{-2}$. Here, U_da is a constant magnetron voltage during a pulse or discharge (5-cont regime), S_da is the average target power density in a pulse and t_in is the duration of the initial rise in the target current (see figure 2). $R_\mathrm{t}(t)$ is the reduction factor of the flux of reactive gas atoms and molecules onto the target due to gas rarefaction and ionization; F_t and F_s are the overfilling factors of the reactive gas on the target side and the substrate side, respectively, of the reactive gas inlets; $B_\mathrm{m}(t)$ and $B_\mathrm{r}(t)$ are the probabilities of ionization and subsequent return of sputtered metal atoms and reactive gas atoms, respectively, onto the target, and $D_\mathrm{t}(t)$ and $D_\mathrm{s}(t)$ are the probabilities of dissociation of reactive gas molecules in the flux onto the target and substrate, respectively. During a pulse period, $R_\mathrm{t}(t)$ decreases linearly from $R_\mathrm{t}(0) = 1$ to the given value of $R_\mathrm{t}(t_\mathrm{in})$ for $t = t_\mathrm{in}$, then it remains constant till $t = t_\mathrm{on}$ and finally $R_\mathrm{t}(t) = 1$ for $t_\mathrm{on} < t \leq T_\mathrm{p}$. $B_\mathrm{m}(t)$ and $B_\mathrm{r}(t)$ increase linearly from $B_\mathrm{m}(0) = 2B_\mathrm{r}(0) = 0$ to the given values $B_\mathrm{m}(t_\mathrm{in}) = 2B_\mathrm{r}(t_\mathrm{in}) = B(t_\mathrm{in})$ for $t = t_\mathrm{in}$, then they remain constant till $t = t_\mathrm{on}$ and finally $B_\mathrm{m}(t) = 2B_\mathrm{r}(t) = 0$ for $t_\mathrm{on} < t \leq T_\mathrm{p}$. $D_\mathrm{t}(t)$ and $D_\mathrm{s}(t)$ increase linearly from $D_\mathrm{t}(0) = D_\mathrm{s}(0) = 0$ to the given values $D_\mathrm{t}(t_\mathrm{in}) = D_\mathrm{s}(t_\mathrm{in}) = D(t_\mathrm{in})$ for $t = t_\mathrm{in}$, then they remain constant till $t = t_\mathrm{on} + t_\mathrm{ac}$, where $t_\mathrm{ac} = 25\,\mu\mathrm{s}$ is an assumed duration of plasma activation after pulse, and finally they decrease exponentially as $D_\mathrm{t}(t) = D_\mathrm{s}(t) = D(t_\mathrm{in})\exp[-\frac{t-(t_\mathrm{on}+t_\mathrm{ac})}{\tau}]$ with $\tau = 434.3\,\mu\mathrm{s}$ for $t_\mathrm{on} + t_\mathrm{ac} < t < T_\mathrm{p}$.

Regime	U_da (V)	S_da (Wcm^{-2})	t_in (μs)	$R_\mathrm{t}(t_\mathrm{in})$	F_t	F_s	$B(t_\mathrm{in})$	$D(t_\mathrm{in})$
5-cont	300	–	–	1.0	1.0	1.0	0.05	0.05
5-200-T	405	50	125	0.9	2.0	1.2	0.20	0.20
5-200-S	350	50	125	0.9	1.0	2.0	0.20	0.20
50-200-T	485	500	25	0.5	2.0	1.2	0.50	0.40
50-200-S	500	500	25	0.5	1.0	2.0	0.50	0.40
50-50-T	600	2000	25	0.2	2.0	1.2	0.60	0.80
50-50-S	675	2000	25	0.2	1.0	2.0	0.60	0.80

fractions of 38.6 % and 43.2 % in table 4), due to the high values of Γ_it during the pulses, at decreased chemisorption fluxes of oxygen particles $\Gamma_\mathrm{ch}^\mathrm{t}$ on the target surface (see the reduction factors $R_\mathrm{t}(t_\mathrm{in}) = 0.5$ and 0.2, and $F_\mathrm{t} = 1.0$ in equation (3)). As expected, an increased flux of the oxygen particles onto the target ($F_\mathrm{t} = 2.0$) at the to-target O_2 inlet leads to increasing chemisorption fluxes $\Gamma_\mathrm{ch}^\mathrm{t}$. As a result, the compound fractions in the target surface layer increase up to $\Theta_\mathrm{ts}(t) \leq 16\,\%$ and $\Theta_\mathrm{ts} < 22\,\%$ for the pulse durations $t_\mathrm{on} = 200\,\mu\mathrm{s}$ and $t_\mathrm{on} = 50\,\mu\mathrm{s}$, respectively.

As can be seen in figure 4, the compound fractions in the substrate surface layers, Θ_s, are systematically higher for the to-substrate O_2 inlet than for the to-target O_2 inlet at the same pulse durations. The main reason is an increased flux of the oxygen particles onto the substrate ($F_\mathrm{s} = 2.0$) resulting in higher chemisorption

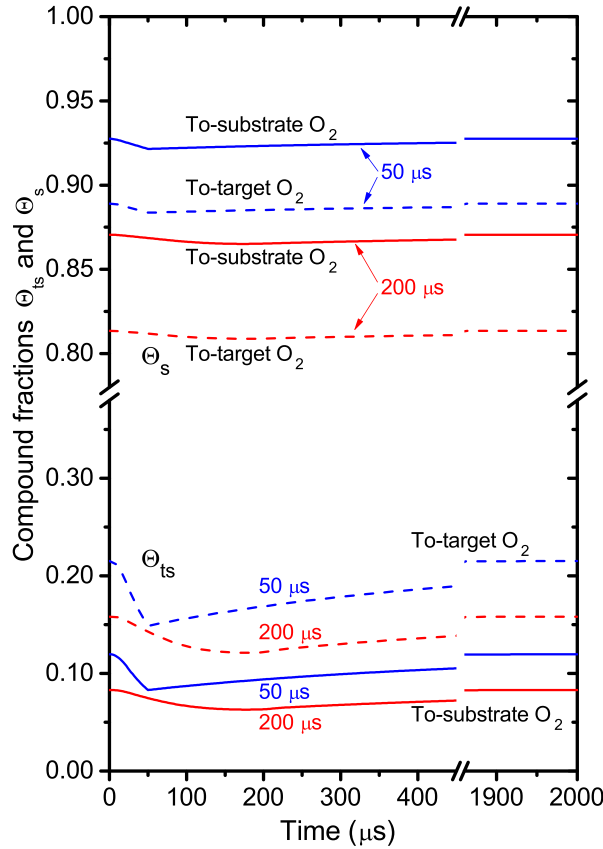

Figure 4. Time evolution of the compound fractions in the target surface layer, $\Theta_{\mathrm{ts}}(t)$, and in the substrate surface layer, $\Theta_{\mathrm{s}}(t)$, calculated using the basic set of internal discharge parameters (table 3) for a pulse period $T_{\mathrm{p}} = 2000\,\mu$s after stabilization of the sputtering process at a fixed oxygen partial pressure $p_{\mathrm{rm}} = 0.05$ Pa, a deposition-averaged target power density $\langle S_{\mathrm{d}}\rangle = 50\,\mathrm{Wcm}^{-2}$ and pulse durations $t_{\mathrm{on}} = 50\,\mu$s and $200\,\mu$s with the to-target O_2 inlet (dashed lines) and the to-substrate O_2 inlet (solid lines).

fluxes $\Gamma^{\mathrm{s}}_{\mathrm{ch}}$ given by equation (17).

In all cases considered, the corresponding values of Θ_{ts} and Θ_{s} are higher at $t_{\mathrm{on}} = 50\,\mu$s than at $t_{\mathrm{on}} = 200\,\mu$s. For Θ_{ts}, this is mostly a consequence of higher chemisorption fluxes $\Gamma^{\mathrm{t}}_{\mathrm{ch}}$ due to a substantially increased dissociation probability $D_{\mathrm{t}}(t_{\mathrm{in}}) = D_{\mathrm{s}}(t_{\mathrm{in}})$ from 0.4 up to 0.8 (table 3) at $t_{\mathrm{on}} = 50\,\mu$s when the average target power density is 4 times higher in a pulse ($S_{\mathrm{da}} = 2000\,\mathrm{Wcm}^{-2}$) than at $t_{\mathrm{on}} = 200\,\mu$s when $S_{\mathrm{da}} = 500\,\mathrm{Wcm}^{-2}$. In addition, absolute values of I_{kir} and I_{spr}, decreasing Θ_{ts}, are reduced at $t_{\mathrm{on}} = 50\,\mu$s compared with $t_{\mathrm{on}} = 200\,\mu$s, as Γ_{it}, appearing in equations (11) and (15), respectively, is on average less than 4 times higher during the pulses at $t_{\mathrm{on}} = 50\,\mu$s than at $t_{\mathrm{on}} = 200\,\mu$s owing to a higher U_{da} (table 3) at the same $\langle S_{\mathrm{d}}\rangle = 50\,\mathrm{Wcm}^{-2}$. For Θ_{s}, higher chemisorption fluxes $\Gamma^{\mathrm{s}}_{\mathrm{ch}}$ due to the enlarged dissociation probability $D_{\mathrm{s}}(t_{\mathrm{in}}) = 0.8$ are combined with reduced deposition fluxes of the zirconium atoms sputtered from the target, $\Gamma^{\mathrm{s}}_{\mathrm{dem}}$, at $t_{\mathrm{on}} = 50\,\mu$s (see the

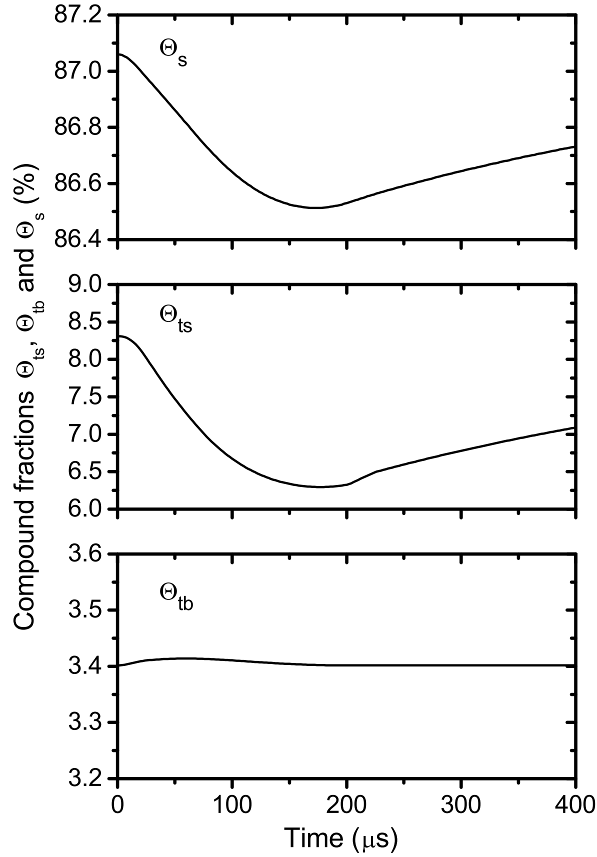

Figure 5. Parts of the time evolution of the compound fractions in the target surface layer, $\Theta_{\rm ts}(t)$, the target bulk layer, $\Theta_{\rm tb}(t)$, and the substrate surface layer, $\Theta_{\rm s}(t)$, calculated using the basic set of internal discharge parameters (table 3) for a pulse period $T_{\rm p} = 2000\,\mu$s after stabilization of the sputtering process at a fixed oxygen partial pressure $p_{\rm rm} = 0.05\,$Pa, a deposition-averaged target power density $\langle S_{\rm d}\rangle = 50\,$Wcm^{-2} and a pulse duration $t_{\rm on} = 200\,\mu$s with the to-substrate O_2 inlet.

increased $\Theta_{\rm ts}$ and $B_{\rm m}(t_{\rm in}) = 0.6$, and the mentioned less than 4 times higher $\Gamma_{\rm it}$ values in equation (19)). As a result, the differences between the corresponding values of $\Theta_{\rm s}$ at $t_{\rm on} = 50\,\mu$s and $t_{\rm on} = 200\,\mu$s are slightly (by 2 %) higher than those between the corresponding values of $\Theta_{\rm ts}$.

Table 4 shows that the chemisorption of oxygen particles during a pulse-off time becomes a dominant process increasing the oxygen content in the target surface layer for the 50-50-T regime and the 50-50-S regime at $p_{\rm rm} = 0.05\,$Pa with the $I_{\rm ch,off}$ fractions of 50.9 % and 53.5 %, respectively. This can be explained by a relatively high value of the dissociation probability $D_{\rm t}(t)$ in the pulse-off time. Let us recall that $D_{\rm t}(t_{\rm in}) = 0.8$ only in the second half of the short $50\,\mu$s pulses, then it remains constant for $25\,\mu$s and finally it decreases relatively slowly (10 times) for $75\,\mu{\rm s} \le t \le 1075\,\mu$s (table 3). As can be seen in table 4, the transfer of oxygen atoms into the target surface layer due to the exposure of the compound from the target bulk layer with the $I_{\rm exp}$ fractions ranging from 44.6 % to 61.8 % is an important

Table 4. Fractions of the individual processes that contribute to the increase (first 4 columns) and decrease (last 2 columns) of the oxygen content in the target surface layer (equation (1)) during various discharge regimes after stabilization of the sputtering process at a fixed oxygen partial pressure $p_{\mathrm{rm}} = 0.05\,\mathrm{Pa}$. The contributions of the individual processes are calculated using equations (22)–(24). Here, $I_{\mathrm{ch,on}}$ and $I_{\mathrm{ch,off}}$ represent the chemisorption of oxygen particles during the pulse-on and pulse-off time, respectively, I_{exp} represents the transfer of oxygen atoms into the target surface layer due to the exposure of the compound from the target bulk layer, and I_{disr} represents the direct implantation of oxygen ions into the target surface layer. The processes decreasing the oxygen content in the target surface layer are the sputtering of oxygen atoms, characterized by I_{spr}, and the knock-on implantation of oxygen atoms into the target bulk layer, characterized by I_{kir}.

	Increase of Θ_{ts}				Decrease of Θ_{ts}	
Regime	$I_{\mathrm{ch,on}}$ (%)	$I_{\mathrm{ch,off}}$ (%)	I_{exp} (%)	I_{disr} (%)	I_{spr} (%)	I_{kir} (%)
5-cont	35.7	0.0	61.8	2.5	41.9	58.1
5-200-T	11.8	28.6	56.6	3.0	44.6	55.4
5-200-S	11.6	25.2	61.4	1.8	37.7	62.3
50-200-T	8.1	30.8	59.4	1.7	39.0	61.0
50-200-S	8.4	32.0	58.8	0.8	38.6	61.4
50-50-T	1.5	50.9	46.8	0.8	42.3	57.7
50-50-S	1.6	53.5	44.6	0.3	43.2	56.8

process contributing to the increase of Θ_{ts} in all cases investigated. As expected, the effect of the direct implantation of oxygen ions into the thin target surface layer on the compound fraction Θ_{ts} is almost negligible ($I_{\mathrm{disr}} \leq 3.0\,\%$).

Table 5 shows that the knock-on implantation of oxygen atoms from the target surface layer with the I_{kir} fractions between 69.9 % and 89.4 % is a more effective process increasing the oxygen content in the target bulk layer at $p_{\mathrm{rm}} = 0.05\,\mathrm{Pa}$ than the direct implantation of oxygen ions with the I_{dibr} fractions between 30.1 % and 10.6 %. As can be seen in table 5, the effect of the direct implantation of zirconium ions on the decrease of Θ_{tb} gradually rises with the growing S_{da} from $5\,\mathrm{Wcm^{-2}}$ (the 5-cont regime) to $2000\,\mathrm{Wcm^{-2}}$ (table 3). The I_{dibm} fractions increase from 9.0 % to 54.1 % at the expense of the I_{exp} fractions (from 91.0 % to 45.9 %). Taking into account that the direct implantation flux of zirconium ions $\Gamma^{\mathrm{t}}_{\mathrm{dibm}}$, given by equation (13), is proportional to the fraction of ionized sputtered zirconium atoms in the ion flux onto the target, $m_{\mathrm{t}}(t)$, expressed by equation (10), it is easy to understand the evolution of I_{dibm}. Let us recall the corresponding increase in $B_{\mathrm{m}}(t_{\mathrm{in}})$, appearing in equation (10), from 0.05 to 0.60 (table 3).

Table 6 shows that the chemisorption of oxygen particles during a pulse-off time with the $I_{\mathrm{ch,off}}$ fractions between 66.7 % and 91.8 % is a highly dominant process increasing the oxygen content in the substrate surface layer at $p_{\mathrm{rm}} = 0.05\,\mathrm{Pa}$ in all pulsed discharge regimes considered. The substantially enlarged $I_{\mathrm{ch,on}}/I_{\mathrm{ch,off}}$ ratios

Table 5. Fractions of the individual processes that contribute to the increase and decrease of the oxygen content in the target bulk layer (equation (2)) during various discharge regimes after stabilization of the sputtering process at a fixed oxygen partial pressure $p_{\mathrm{rm}} = 0.05\,\mathrm{Pa}$. The contributions of the individual processes are calculated using equation (22). Here, I_{kir} and I_{dibr} represent the knock-on implantation of oxygen atoms from the target surface layer and the direct implantation of oxygen ions, respectively. The processes decreasing the oxygen content in the target bulk layer are the transfer of oxygen atoms into the target surface layer due to the exposure of the compound from the target bulk layer, characterized by I_{exp}, and the direct implantation of zirconium ions, characterized by I_{dibm}.

Regime	Increase of Θ_{tb}		Decrease of Θ_{tb}	
	I_{kir} (%)	I_{dibr} (%)	I_{exp} (%)	I_{dibm} (%)
5-cont	89.4	10.6	91.0	9.0
5-200-T	83.5	16.5	71.7	28.3
5-200-S	86.9	13.1	71.8	28.2
50-200-T	69.9	30.1	50.5	49.5
50-200-S	71.2	28.8	50.5	49.5
50-50-T	80.8	19.2	45.9	54.1
50-50-S	83.7	16.3	45.9	54.1

found for the chemisorption of oxygen particles on the substrates surface (table 6) than on the target surface (table 4) at the corresponding high power 50-200 and 50-50 discharge regimes are mainly due to the higher sticking coefficient of oxygen molecules on the substrate surface $\alpha^{\mathrm{s}}_{\mathrm{rm}} = 0.5$ than on the target surface $\alpha^{\mathrm{t}}_{\mathrm{rm}} = 0.2$ in a pulse-on time (section 3.2). As can be seen in table 6, the effect of the deposition of oxygen atoms sputtered from the target on the compound fraction Θ_{s} is almost negligible ($I_{\mathrm{der}} \leq 2.1\,\%$).

3.3.1.2. Various fixed oxygen partial pressures Figures 6–8 present the compound fractions in the target and substrate surface layers at the end of the pulse period $T_{\mathrm{p}} = 2000\,\mu\mathrm{s}$ after stabilization of the sputtering process during different discharge regimes (table 3) at various fixed oxygen partial pressures. The sensitivity of the results obtained to small changes in the internal discharge parameters is shown in figures 7 and 8.

In figure 6, we compare the stabilized compound fractions Θ_{ts} and Θ_{s} obtained for the low power 5-200-T and 5-200-S regimes, and for the continuous 5-cont regime performed at the same target power density of $5\,\mathrm{Wcm}^{-2}$ during a deposition. As expected (see equations (3) and (17)), Θ_{ts} and Θ_{s} increase with an increasing p_{rm}, appearing in equation (4), for all discharge regimes. For the 5-200-T regime, we obtained systematically higher values of Θ_{ts} mainly due to an increased flux of oxygen particles onto the target ($F_{\mathrm{t}} = 2.0$ and $F_{\mathrm{s}} = 1.2$) than for the 5-200-S regime,

Table 6. Fractions of the individual processes that contribute to the increase of the oxygen content in the substrate surface layer (equation (16)) during various discharge regimes after stabilization of the sputtering process at a fixed oxygen partial pressure $p_{\rm rm} = 0.05\,{\rm Pa}$. The contributions of the individual processes are calculated using equations (22)–(24). Here, $I_{\rm ch,on}$ and $I_{\rm ch,off}$ represent the chemisorption of oxygen particles during the pulse-on and pulse-off time, respectively, and $I_{\rm der}$ represents the deposition of oxygen atoms sputtered from the target. These processes are balanced by the deposition of the zirconium atoms sputtered from the target, characterized by $I_{\rm dem}$.

Regime	$I_{\rm ch,on}$ (%)	$I_{\rm ch,off}$ (%)	$I_{\rm der}$ (%)
5-cont	97.9	0.0	2.1
5-200-T	25.4	73.0	1.6
5-200-S	25.3	74.1	0.6
50-200-T	31.7	66.7	1.6
50-200-S	31.3	68.2	0.5
50-50-T	7.8	91.0	1.2
50-50-S	7.8	91.8	0.4

when we obtained systematically higher values of $\Theta_{\rm s}$ mainly due to an increased flux of oxygen particles onto the substrate ($F_{\rm t} = 1.0$ and $F_{\rm s} = 2.0$). Substantially reduced (by 11 % – 17 %) values of $\Theta_{\rm ts}$ for the 5-200-S regime compared with the 5-cont regime are the result of a complicated interplay between the knock-on implantation flux $\Gamma^{\rm t}_{\rm kir}$ and the sputtering flux $\Gamma^{\rm t}_{\rm spr}$, which decrease $\Theta_{\rm ts}$, and the transfer flux due to exposure $\Gamma^{\rm t}_{\rm exp}$ and the chemisorption flux $\Gamma^{\rm t}_{\rm ch}$, which are the dominant processes increasing $\Theta_{\rm ts}$ (equation (1) and table 4). It should be noted that the ion flux $\Gamma_{\rm it}$, appearing in equations (11), (15) and (5) for $\Gamma^{\rm t}_{\rm kir}$, $\Gamma^{\rm t}_{\rm spr}$ and $\Gamma^{\rm t}_{\rm exp}$, respectively, is on average 8.6 times higher (see $U_{\rm da}$ in table 3) during pulse-on time in the 5-200-S regime than in the 5-cont regime and that the chemisorption flux $\Gamma^{\rm t}_{\rm ch}$, given by equation (3), is decreased by the reduction factor $R_{\rm t}(t)$, with $R_{\rm t}(t_{\rm in}) = 0.9$, and enlarged by the dissociation probability $D_{\rm t}(t)$, with $D_{\rm t}(t_{\rm in}) = 0.2$, in the 5-200-S regime (table 3).

As can be seen in figure 6, the compound fractions $\Theta_{\rm s}$ obtained for both pulsed 5-200 regimes are slightly higher than for the 5-cont regime. This can be explained by a higher chemisorption flux $\Gamma^{\rm s}_{\rm ch}$, given by equation (17), due to the increased dissociation probability $D_{\rm s}(t)$, with $D_{\rm s}(t_{\rm in}) = 0.2$, and the enlarged sticking coefficient $\alpha^{\rm s}_{\rm rm} = 0.5$ for $t \leq t_{\rm on} + t_{\rm ac}$ at a reduced deposition flux of zirconium atoms sputtered from the target, $\Gamma^{\rm s}_{\rm dem}$, given by equation (19), due to the increased $B_{\rm m}(t)$, with $B_{\rm m}(t_{\rm in}) = 0.2$. For the 5-200-S regime, $F_{\rm s} = 2.0$ (table 3) and a systematically lower $\Theta_{\rm ts}$ (figure 6) increase the values of $\Gamma^{\rm s}_{\rm ch}$ and $\Gamma^{\rm s}_{\rm dem}$, respectively.

Figure 7 shows the stabilized compound fractions $\Theta_{\rm ts}$ and $\Theta_{\rm s}$ for the high power 50-200-T and 50-200-S regimes. A rise in $S_{\rm da}$ from $50\,{\rm Wcm^{-2}}$ for the 5-200 regimes (figure 6) to $500\,{\rm Wcm^{-2}}$ for the 50-200 regimes is accompanied by the

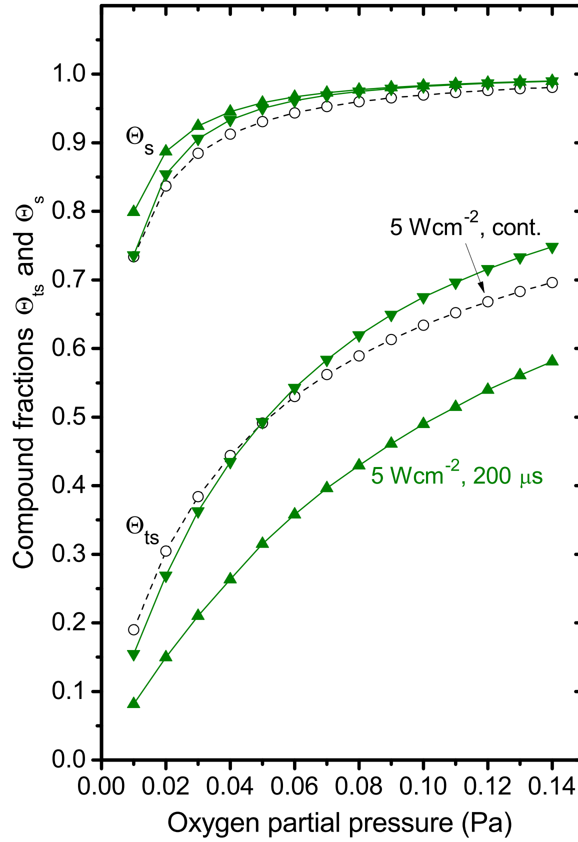

Figure 6. The compound fractions in the target surface layer, $\Theta_{\rm ts}$, and in the substrate surface layer, $\Theta_{\rm s}$, calculated using the basic set of internal discharge parameters (table 3) for the end of the pulse period $T_{\rm p} = 2000\,\mu$s after stabilization of the sputtering process at various fixed oxygen partial pressures, a deposition-averaged target power density $\langle S_{\rm d}\rangle = 5\,{\rm Wcm}^{-2}$ and a pulse duration $t_{\rm on} = 200\,\mu$s with the to-target O_2 inlet (downward triangles) and the to-substrate O_2 inlet (upward triangles). For comparison, the corresponding stabilized values (circles) of $\Theta_{\rm ts}$ and $\Theta_{\rm s}$ obtained for a continuous dc reactive sputtering at a target power density of $5\,{\rm Wcm}^{-2}$ are also given.

corresponding increase in the ion flux $\Gamma_{\rm it}$ (on average 8.4 times and 7.0 times for the 50-200-T and the 50-200-S regime, respectively) and by the changes in the internal discharge parameters $R_{\rm t}(t_{\rm in})$ from 0.9 to 0.5, $B_{\rm m}(t_{\rm in}) = 2B_{\rm r}(t_{\rm in})$ from 0.2 to 0.5, and $D_{\rm t}(t_{\rm in}) = D_{\rm s}(t_{\rm in})$ from 0.2 to 0.4 (table 3).

As can be seen in figure 7, the significant increase of $\Gamma_{\rm it}$ during the 50-200 regimes at the same values of $R_{\rm t}(t_{\rm in}) = 0.9$, $B_{\rm m}(t_{\rm in}) = 2B_{\rm r}(t_{\rm in}) = 0.2$ and $D_{\rm t}(t_{\rm in}) = D_{\rm s}(t_{\rm in}) = 0.2$ as for the 5-200 regimes leads to a rapid decrease of the compound fraction $\Theta_{\rm ts}$ (see empty triangles in figure 7 and full triangles in figure 6). A further, but much smaller, contribution to the decrease of $\Theta_{\rm ts}$ to the values $\Theta_{\rm ts} \leq 16\,\%$ and even $\Theta_{\rm ts} \leq 8\,\%$ (see full triangles) during a pulse period at $p_{\rm rm} = 0.05\,$Pa for the 50-200-T regime and the 50-200-S regime, respectively, is caused by a further increase in the knock-on implantation flux $\Gamma^{\rm t}_{\rm kir}$, given by equation

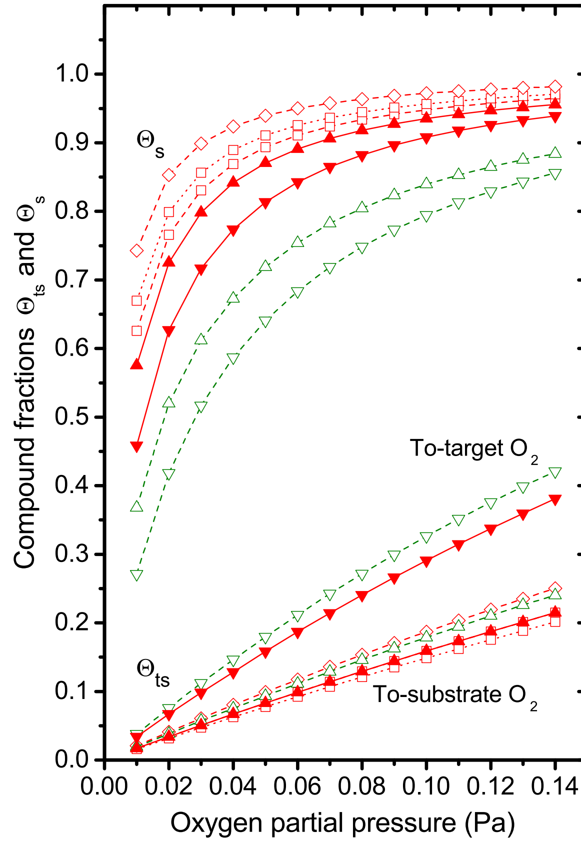

Figure 7. The compound fractions in the target surface layer, Θ_{ts}, and in the substrate surface layer, Θ_{s}, calculated for the end of the pulse period $T_{\mathrm{p}} = 2000\,\mu\mathrm{s}$ after stabilization of the sputtering process at various fixed oxygen partial pressures, a deposition-averaged target power density $\langle S_{\mathrm{d}} \rangle = 50\,\mathrm{Wcm}^{-2}$ and a pulse duration $t_{\mathrm{on}} = 200\,\mu\mathrm{s}$ with the to-target O_2 inlet (downward triangles) and the to-substrate O_2 inlet (upward triangles, squares and diamonds). The values of Θ_{ts} and Θ_{s} for $\langle S_{\mathrm{d}} \rangle = 50\,\mathrm{Wcm}^{-2}$ and $t_{\mathrm{on}} = 200\,\mu\mathrm{s}$ obtained using the basic set of internal discharge parameters (table 3) for $\langle S_{\mathrm{d}} \rangle = 50\,\mathrm{Wcm}^{-2}$ and $5\,\mathrm{Wcm}^{-2}$ at $t_{\mathrm{on}} = 200\,\mu\mathrm{s}$ are marked by the full and empty triangles, respectively. The dashed lines with squares, dotted lines with squares and dashed lines with diamonds represent the values of Θ_{ts} and Θ_{s} obtained using the basic set of internal discharge parameters for $\langle S_{\mathrm{d}} \rangle = 50\,\mathrm{Wcm}^{-2}$ and $t_{\mathrm{on}} = 200\,\mu\mathrm{s}$, but with (dashed lines with squares) $F_{\mathrm{s}} = 2.5$, with (dotted lines with squares) $F_{\mathrm{s}} = 2.5$ and $B_{\mathrm{m}}(t_{\mathrm{in}}) = 2B_{\mathrm{r}}(t_{\mathrm{in}}) = 0.6$, and with (dashed lines with diamonds) $F_{\mathrm{s}} = 2.5$, $B_{\mathrm{m}}(t_{\mathrm{in}}) = 2B_{\mathrm{r}}(t_{\mathrm{in}}) = 0.6$ and $D_{\mathrm{t}}(t_{\mathrm{in}}) = D_{\mathrm{s}}(t_{\mathrm{in}}) = 0.6$, respectively.

(11), due to a lower Θ_{tb}, which is reduced by an enlarged direct implantation flux $\Gamma^{\mathrm{t}}_{\mathrm{dibm}}$ when $B_{\mathrm{m}}(t_{\mathrm{in}})$ increases from 0.2 to 0.5 (see equations (13) and (10)). Taking into account the opposite effect of the decreased $R_{\mathrm{t}}(t_{\mathrm{in}})$ from 0.9 to 0.5 and the increased $D_{\mathrm{t}}(t_{\mathrm{in}})$ from 0.2 to 0.4 on the chemisorption flux $\Gamma^{\mathrm{t}}_{\mathrm{ch}}$, given by equation (3), we believe that the simultaneous changes in $R_{\mathrm{t}}(t_{\mathrm{in}})$ and $D_{\mathrm{t}}(t_{\mathrm{in}})$ have only a very small influence on the compound fractions Θ_{ts} determined. In contrast, a higher chemisorption flux $\Gamma^{\mathrm{s}}_{\mathrm{ch}}$, given by equation (17), due to the increased $D_{\mathrm{s}}(t_{\mathrm{in}})$ from 0.2

to 0.4, and a lower deposition flux of zirconium atoms sputtered from the target, Γ^{s}_{dem}, given by equation (19), due to the increased $B_{m}(t_{in})$ from 0.2 to 0.5 at the same Γ_{it}, result in a significant rise in Θ_{s} (see full triangles).

As shown in figure 7, an increased flux of the oxygen particles onto the substrate ($F_{s} = 2.5$), a higher probability of ionization and subsequent return of sputtered zirconium atoms onto the target ($B_{m}(t_{in}) = 0.6$), and a higher probability of dissociation of oxygen molecules particularly in the flux onto the substrate ($D_{s}(t_{in}) = 0.6$) and to a much smaller extent also in the flux onto the target ($D_{t}(t_{in}) = 0.6$), lead to a further increase in the compound fraction Θ_{s} for the 50-200-S regime. Except for $D_{t}(t_{in}) = 0.6$, these changes in the internal discharge parameters for the 50-200-S regime (table 3) result in very small changes in the compound fraction Θ_{ts}. The higher $D_{t}(t_{in}) = 0.6$ increases Θ_{ts} due to a higher chemisorption flux Γ^{t}_{ch}. As a consequence, Θ_{s} increases due to a lower deposition flux Γ^{s}_{dem}.

Let us recall that the very low values of Θ_{ts} achieved for the 50-200-S regime are of key importance for the reactive HiPIMS deposition of stoichiometric ZrO_2 films, as they make it possible to improve the quality of the films due to a minimized arcing and production of O^{-} ions on the target surface, and to enhance significantly the deposition rate of films due to intense sputtering of zirconium atoms from a large metallic part of the target [21].

Figure 8 shows the stabilized compound fractions Θ_{ts} and Θ_{s} for the 50-50-T and 50-50-S regimes. A rise in S_{da} from 500 Wcm^{-2} for the 50-200 regimes (figure 7) to 2000 Wcm^{-2} for the 50-50 regimes with shortened voltage pulses (from 200 μs to 50 μs) is accompanied by the corresponding increase in the ion flux Γ_{it} (on average 3.2 times and 3.0 times for the 50-50-T regime and the 50-50-S regime, respectively) and by the changes in the internal discharge parameters $R_{t}(t_{in})$ from 0.5 to 0.2, $B_{m}(t_{in}) = 2B_{r}(t_{in})$ from 0.5 to 0.6, and $D_{t}(t_{in}) = D_{s}(t_{in})$ from 0.4 to 0.8 (table 3).

As can be seen in figure 8, the significant increase of Γ_{it} during the 50 μs pulses at the same values of $R_{t}(t_{in}) = 0.5$, $B_{m}(t_{in}) = 2B_{r}(t_{in}) = 0.5$ and $D_{t}(t_{in}) = D_{s}(t_{in}) = 0.4$ as for the 50-200 regimes (table 3) leads to almost the same values of Θ_{ts} (see empty triangles) as for the 50-200 regimes (see full triangles in figure 7). However, the values of Θ_{s} calculated under these conditions (see empty triangles) are systematically lower than for the 50-200 regimes (see full triangles in figure 7). The use of the parameters $R_{t}(t_{in}) = 0.2$, $B_{m}(t_{in}) = 2B_{r}(t_{in}) = 0.6$ and $D_{t}(t_{in}) = D_{s}(t_{in}) = 0.8$ resulted in a considerable rise (see full triangles in figure 8) in Θ_{ts}, caused mainly by a higher chemisorption flux Γ^{t}_{ch} due to the enlarged $D_{t}(t)$, and in Θ_{s}, caused mainly by a higher chemisorption flux Γ^{s}_{ch} due to the enlarged $D_{s}(t)$ and by a lower deposition rate Γ^{s}_{dem} due to the higher $B_{m}(t)$. In all cases considered, the corresponding resulting values obtained for Θ_{ts} and Θ_{s} are higher at $t_{on} = 50\,\mu$s than at $t_{on} = 200\,\mu$s, as presented for $p_{rm} = 0.05$ Pa in figure 4 and discussed before.

As shown in figure 8, an increased flux of the oxygen particles onto the substrate

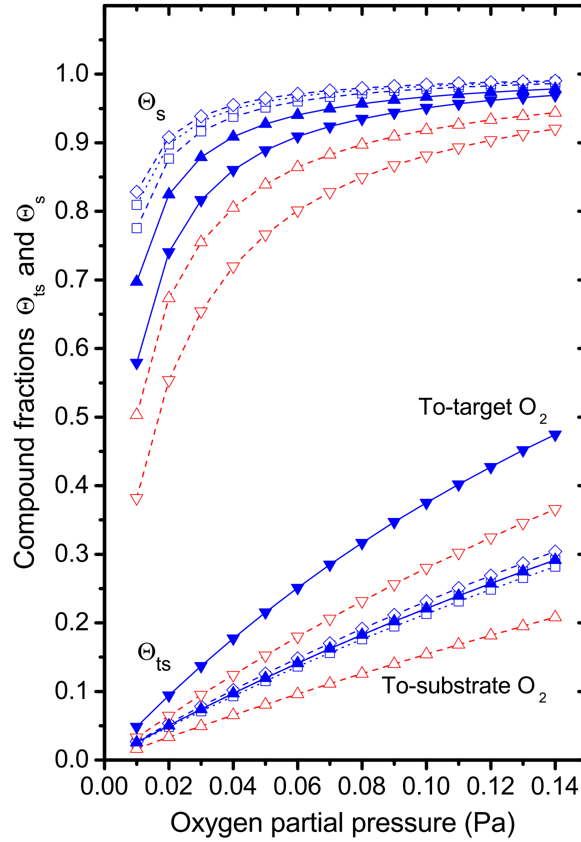

Figure 8. The compound fractions in the target surface layer, Θ_{ts}, and in the substrate surface layer, Θ_{s}, calculated for the end of the pulse period $T_{\mathrm{p}} = 2000\,\mu\mathrm{s}$ after stabilization of the sputtering process at various fixed oxygen partial pressures, a deposition-averaged target power density $\langle S_{\mathrm{d}} \rangle = 50\,\mathrm{Wcm}^{-2}$ and a pulse duration $t_{\mathrm{on}} = 50\,\mu\mathrm{s}$ with the to-target O_2 inlet (downward triangles) and the to-substrate O_2 inlet (upward triangles, squares and diamonds). The values of Θ_{ts} and Θ_{s} for $\langle S_{\mathrm{d}} \rangle = 50\,\mathrm{Wcm}^{-2}$ and $t_{\mathrm{on}} = 50\,\mu\mathrm{s}$ obtained using the basic set of internal discharge parameters (table 3) for $\langle S_{\mathrm{d}} \rangle = 50\,\mathrm{Wcm}^{-2}$ at $t_{\mathrm{on}} = 50\,\mu\mathrm{s}$ and $200\,\mu\mathrm{s}$ are marked by the full and empty triangles, respectively. The dashed lines with squares, dotted lines with squares and dashed lines with diamonds represent the values of Θ_{ts} and Θ_{s} obtained using the basic set of internal discharge parameters for $\langle S_{\mathrm{d}} \rangle = 50\,\mathrm{Wcm}^{-2}$ and $t_{\mathrm{on}} = 50\,\mu\mathrm{s}$, but with (dashed lines with squares) $F_{\mathrm{s}} = 3.0$, with (dotted lines with squares) $F_{\mathrm{s}} = 3.0$ and $B_{\mathrm{m}}(t_{\mathrm{in}}) = 2B_{\mathrm{r}}(t_{\mathrm{in}}) = 0.7$, and with (dashed lines with diamonds) $F_{\mathrm{s}} = 3.0$, $B_{\mathrm{m}}(t_{\mathrm{in}}) = 2B_{\mathrm{r}}(t_{\mathrm{in}}) = 0.7$ and $D_{\mathrm{t}}(t_{\mathrm{in}}) = D_{\mathrm{s}}(t_{\mathrm{in}}) = 0.9$, respectively.

($F_{\mathrm{s}} = 3.0$), a higher probability of ionization and subsequent return of sputtered zirconium atoms onto the target ($B_{\mathrm{m}}(t_{\mathrm{in}}) = 0.7$), and a higher probability of dissociation of oxygen molecules in the flux onto the substrate ($D_{\mathrm{s}}(t_{\mathrm{in}}) = 0.9$) lead to a further increase in the compound fraction Θ_{s} for the 50-50-S regime. In contrast, these changes (including $D_{\mathrm{t}}(t_{\mathrm{in}}) = 0.9$) in the internal discharge parameters (table 3) result in very small changes in the compound fraction Θ_{ts}.

3.3.2. Deposition rate of films

Figure 9 presents the deposition rates of zirconium atoms deposited on the substrate area A_s, M_s, after stabilization of the sputtering process during different discharge regimes (table 3) at various fixed oxygen partial pressures. Let us recall that the values of M_s, given by equation (25), are directly related to the deposition rates, a_D, of the films produced (equation (26)).

To understand the dependences obtained for M_s, and thus also for a_D (table 2), we simplified formula (25). Substituting for Γ_it from equation (6) into formula (25), we can write

$$M_\mathrm{s} \simeq \frac{t_\mathrm{on}}{T_\mathrm{p}} \frac{J_\mathrm{ta} A_\mathrm{t}}{e(1+\gamma)} Y_\mathrm{mm} \left(1 - \Theta_\mathrm{tsa} + \frac{Y_\mathrm{mc}}{Y_\mathrm{mm}} \Theta_\mathrm{tsa}\right) (1 - B_\mathrm{ma}) f_\mathrm{trm} \,, \qquad (32)$$

where we introduced the pulse-averaged target current density, J_ta, the pulse-averaged compound fraction in the target surface layer, Θ_tsa, and the pulse-averaged probability of ionization and subsequent return of sputtered metal atoms onto the target, B_ma. Using the simple generalized relation $Y_\mathrm{mm} = k_\mathrm{sp} U_\mathrm{da}^{0.5}$, where k_sp is a constant for a given metal [40, 55], and taking into account that $S_\mathrm{da} \simeq U_\mathrm{da} J_\mathrm{ta}$ (see equation (27)), $\langle S_\mathrm{d} \rangle \simeq S_\mathrm{da} t_\mathrm{on}/T_\mathrm{p}$ and $Y_\mathrm{mc}/Y_\mathrm{mm} \leq 0.05$ (see equations (29) and (30)), we can obtain a simplified relation for M_s (and thus also for the deposition rate of films, a_D) applicable to a reactive HiPIMS deposition

$$a_\mathrm{D} = \frac{M_\mathrm{s}}{n_\mathrm{m,c} A_\mathrm{s}} \propto (1 - 0.95\Theta_\mathrm{tsa})(1 - B_\mathrm{ma}) f_\mathrm{trm} \frac{k_\mathrm{sp} U_\mathrm{da}^{-0.5}}{n_\mathrm{m,c}(1+\gamma)} \langle S_\mathrm{d} \rangle \,. \qquad (33)$$

Figure 9 shows the rates M_s calculated using the corresponding basic sets of the internal discharge parameters for all discharge regimes investigated (table 3). Moreover, a high sensitivity of M_s to an increased flux of the oxygen particles onto the target (F_t) and to a higher probability of ionization and subsequent return of sputtered zirconium atoms onto the target (B_m) is presented for the 50-200-T regime ($F_\mathrm{t} = 2.5$ and $B_\mathrm{m}(t_\mathrm{in}) = 2B_\mathrm{r}(t_\mathrm{in}) = 0.6$) and the 50-50-T regime ($F_\mathrm{t} = 3.0$ and $B_\mathrm{m}(t_\mathrm{in}) = 2B_\mathrm{r}(t_\mathrm{in}) = 0.7$). In all cases considered, the values of M_s decrease with an increasing oxygen partial pressure due to an increasing compound fraction Θ_ts (see the increased Θ_tsa in relation (32) or (33), and figures 6 – 8). The corresponding values of M_s are systematically higher for the to-substrate O_2 inlet than for the to-target O_2 inlet due to lower values of Θ_ts (figures 6 – 8). As expected, the increased F_t and B_m result in a decrease of M_s (see the increased Θ_tsa and B_ma in relation (32) or (33)).

Taking into account that the mass density of the deposited stoichiometric ZrO_2 films was close to that for a bulk material [21] and that the compound fraction on the substrate calculated by the model is close to unity, we can use equation (26) to compare the calculated and measured deposition rates of the films using a fixed $n_\mathrm{m,c} = 2.78 \times 10^{22}\,\mathrm{cm}^{-3}$ determined from the bulk density of ZrO_2. Let us note again, that the experiments were carried out using a pulsed (i.e., not continuous) reactive gas (oxygen) flow control, but the model calculations were carried out for

a fixed oxygen partial pressure. For the comparison of the deposition rates we used $p_{\mathrm{rm}} = 0.05\,\mathrm{Pa}$ for all discharge regimes.

For the 50-200-S regime, the deposition rate of 118 nm/min calculated for the basic internal discharge parameters is equal to the measured value (see table 2), as the transport factor $f_{\mathrm{trm}} = f_{\mathrm{trr}}$ used in this work was determined using the deposition rate measured for this regime. For the 50-200-T regime, the calculated deposition rate is in the range of $111-89$ nm/min, where the first value corresponds to the basic internal discharge parameters (see table 3) while the second value was obtained with $F_{\mathrm{t}} = 2.5$ and $B_{\mathrm{m}}(t_{\mathrm{in}}) = 2B_{\mathrm{r}}(t_{\mathrm{in}}) = 0.6$ (see full diamonds in figure 9). The measured deposition rate of 62 nm/min is, however, lower than the calculated range. This indicates that in reality, there might be a higher flux of oxygen onto the target than assumed due to the proximity of the reactive gas inlet to the target and its orientation toward the target. Also larger differences in B_{m} might be expected between the to-target and to-substrate regimes due to the changes in the discharge plasma.

For the 50-50-S regime, the calculated deposition rate of 92 nm/min (see M_{s} in figure 9) is in good agreement with the measured value of 80 nm/min. Again, a larger disagreement is observed for the 50-50-T regime for which the calculated values of $87-65$ nm/min corresponding to the M_{s} interval in figure 9 are significantly higher than the measured value of 15 nm/min.

For the 5-200-S and 5-200-T regimes, the deposition rates calculated for the basic internal discharge parameters are of 16 and 11 nm/min, respectively. In the case of the 5-200-T, the measured value of $a_{\mathrm{D}} = 11$ nm/min is in excellent agreement with the calculated value. As mentioned in section 3.1, the very low value of $a_{\mathrm{D}} = 5$ nm/min measured for the 5-200-S regime cannot be compared with the calculated value.

A slight increase in M_{s} achieved for the 5-200-S regime, compared with the 5-cont regime (figure 9), is a result of the significantly decreased Θ_{ts} (see the decreased Θ_{tsa} in relation (32) or (33) and figure 6) at the increased $B_{\mathrm{m}}(t_{\mathrm{in}})$ from 0.05 to 0.20 and the increased U_{da} from 300 V to 350 V (table 3).

4. Conclusions

We present a time-dependent parametric model for reactive HiPIMS deposition of films. The model takes into account specific features of HiPIMS discharges, namely, gas rarefaction and ionization in front of the sputtered target, backward flux of the ionized sputtered metal atoms and reactive gas atoms onto the target, and high degree of dissociation of reactive gas molecules in the fluxes onto the target and substrate. Moreover, the model can account for a possible increase in the density of the reactive gas in front of the reactive gas inlets placed between the target and the substrate.

The model makes it possible to calculate the compound fractions in two target

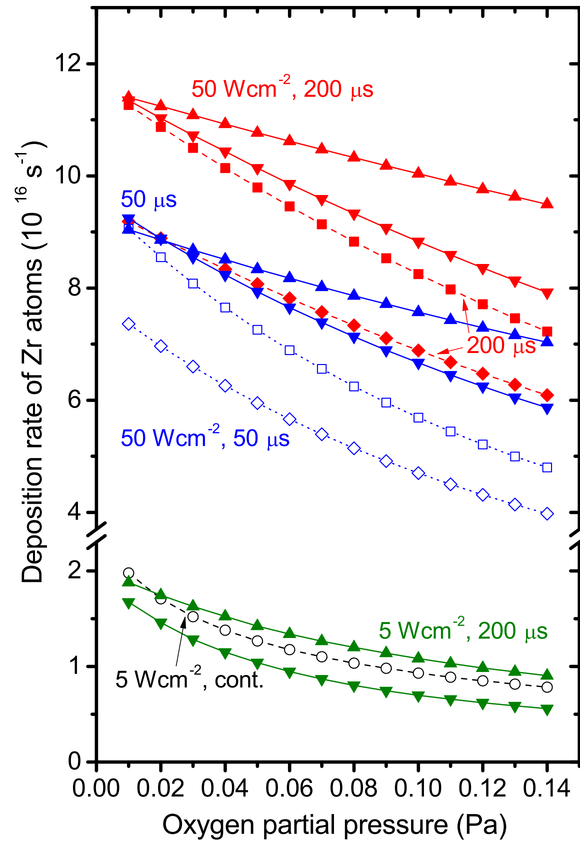

Figure 9. The deposition rate of Zr atoms on the substrate, M_s, calculated after stabilization of the sputtering process at various fixed oxygen partial pressures for $\langle S_d \rangle = 50\,\mathrm{Wcm^{-2}}$ at $t_{on} = 200\,\mu$s and $50\,\mu$s, and $\langle S_d \rangle = 5\,\mathrm{Wcm^{-2}}$ at $t_{on} = 200\,\mu$s with the to-target O_2 inlet (downward triangles, squares and diamonds) and the to-substrate O_2 inlet (upward triangles). The values of M_s obtained using the corresponding basic sets of internal discharge parameters (table 3) are marked by the full triangles. The dashed lines with full squares and diamonds represent the values of M_s obtained using the basic set of internal discharge parameters for $\langle S_d \rangle = 50\,\mathrm{Wcm^{-2}}$ and $t_{on} = 200\,\mu$s, but with (full squares) $F_t = 2.5$, and with (full diamonds) $F_t = 2.5$ and $B_m(t_{in}) = 2B_r(t_{in}) = 0.6$, respectively. The dotted lines with empty squares and diamonds represent the values of M_s obtained using the basic set of internal discharge parameters for $\langle S_d \rangle = 50\,\mathrm{Wcm^{-2}}$ and $t_{on} = 50\,\mu$s, but with (empty squares) $F_t = 3.0$, and with (empty diamonds) $F_t = 3.0$ and $B_m(t_{in}) = 2B_r(t_{in}) = 0.7$, respectively. For comparison, the corresponding stabilized values (circles) of M_s obtained for a continuous dc reactive sputtering at a target power density of $5\,\mathrm{Wcm^{-2}}$ are also given.

layers and in one substrate layer, and the deposition rate of films at fixed partial pressures of the reactive and inert gas. A simplified relation for the deposition rate of films prepared using a reactive HiPIMS is presented.

We used the model to simulate controlled reactive HiPIMS depositions of the stoichiometric ZrO_2 films, which were carried out in our laboratories with two different configurations of the O_2 inlets in front of the sputtered target [21]. Comparing the experimental values obtained for the deposition rate of the films with the corresponding theoretical predictions, we can conclude that our model provides a good qualitative picture of the complicated processes on the target and substrate surfaces, and in the discharge plasma, which determine the deposition mechanisms in the HiPIMS discharges investigated. Only in the case of the to-target O_2 inlet at $\langle S_{\mathrm{d}} \rangle \simeq 50\,\mathrm{Wcm}^{-2}$, particularly for the shorter discharge pulses with $t_{\mathrm{on}} = 50\,\mu\mathrm{s}$, we observed a larger disagreement between the calculated and measured deposition rates of the films. The results achieved might help in the design of new sputter sources, particularly in combination with new reactive gas inlet configurations, and in the choice of their operating conditions.

The highest deposition rate of the ZrO_2 films $a_{\mathrm{D}} = 118\,\mathrm{nm/min}$ was achieved for the target-to-substrate distance $d = 100\,\mathrm{mm}$ at the deposition-averaged target power density $\langle S_{\mathrm{d}} \rangle = 50\,\mathrm{Wcm}^{-2}$ and the pulse duration $t_{\mathrm{on}} = 200\,\mu\mathrm{s}$ with the to-substrate O_2 inlet. Under these conditions, the compound fraction in the target surface layer was very low ($\Theta_{\mathrm{ts}} \lesssim 10\,\%$). This is of key importance not only for intense sputtering of Zr atoms from a large metallic part of the target, but also for a minimized arcing and production of O^- ions on the target surface.

Acknowledgments

This work was supported by the Grant Agency of the Czech Republic under Project No. GA14–03875S.

References

[1] Sarakinos K, Alami J and Konstantinidis S 2010 *Surf. Coat. Technol.* **204** 1661

[2] Lundin D and Sarakinos K 2012 *J. Mater. Res.* **27** 780

[3] Gudmundsson J T, Brenning N, Lundin D and Helmersson U 2012 *J. Vac. Sci. Technol. A* **30** 030801

[4] Bobzin K, Bagcivan N, Immich P, Bolz S, Alami J and Cremer R 2009 *J. Mater. Process. Technol.* **209** 165

[5] Alami J, Sarakinos K, Uslu F and Wuttig M 2009 *J. Phys. D: Appl. Phys.* **42** 015304

[6] Ehiasarian A P, Wen J G and Petrov I 2007 *J. Appl. Phys.* **101** 054301

[7] Greczynski G, Jensen J, Böhlmark J and Hultman L 2010 *Surf. Coat. Technol.* **205** 118

[8] Konstantinidis S, Dauchot J P and Hecq M 2006 *Thin Solid Films* **515** 1182

[9] Sarakinos K, Alami J and Wuttig M 2007 *J. Phys. D: Appl. Phys.* **40** 2108

[10] Straňák V, Quaas M, Wulff H, Hubička Z, Wrehde S, Tichý M and Hippler R 2008 *J. Phys. D: Appl. Phys.* **41** 055202

[11] Amin A, Köhl D and Wuttig M 2010 *J. Phys. D: Appl. Phys.* **43** 405303

[12] Vlček J, Rezek J, Houška J, Čerstvý R and Bugyi R 2013 *Surf. Coat. Technol.* **236** 550

[13] Audronis M, Matthews A, Juškevičius K and Drazdys R 2014 *Vacuum* **107** 159

[14] Vlček J, Belosludtsev A, Rezek J, Houška J, Čapek J, Čerstvý R and Haviar S 2015 *Surf. Coat. Technol.* DOI: 10.1016/j.surfcoat.2015.08.024

[15] Hála M, Čapek J, Zabeida O, Klemberg-Sapieha J E and Martinu L 2012 *J. Phys. D: Appl. Phys.* **45** 055204

[16] Fortier J-P, Baloukas B, Zabeida O, Klemberg-Sapieha J E and Martinu L 2014 *Sol. Energy Mater. Sol. Cells* **125** 291

[17] Sittinger V, Ruske F, Werner W, Jacobs C, Szyszka B and Christie D J 2008 *Thin Solid Films* **516** 5847

[18] Ruske F, Pflug A, Sittinger V, Werner W, Szyszka B and Christie D J 2008 *Thin Solid Films* **516** 4472

[19] Benzeggouta D, Hugon M C and Bretagne J 2009 *Plasma Sources Sci. Technol.* **18** 045026

[20] Hála M, Vernhes R, Zabeida O, Klemberg-Sapieha J E and Martinu L 2014 *J. Appl. Phys.* **116** 213302

[21] Vlček J, Rezek J, Houška J, Kozák T and Kohout J 2015 *Vacuum* **114** 131

[22] Berg S, Blom H-O, Larsson T and Nender C 1987 *J. Vac. Sci. Technol. A* **5** 202

[23] Kadlec S, Musil J and Vyskočil J 1990 *J. Vac. Sci. Technol. A* **8** 1560

[24] Kusano E 1993 *J. Appl. Phys.* **73** 8565

[25] Ershov A and Pekker L 1996 *Thin Solid Films* **289** 140

[26] Berg S and Nyberg T 2005 *Thin Solid Films* **476** 215

[27] Kubart T, Kappertz O, Nyberg T and Berg S 2006 *Thin Solid Films* **515** 421

[28] Möller W and Güttler D 2007 *J. Appl. Phys.* **102** 094501

[29] Strijckmans K and Depla D 2014 *J. Phys. D: Appl. Phys.* **47** 235302

[30] Depla D and De Gryse R 2004 *Surf. Coat. Technol.* **183** 184

[31] Chen Z Y, Bogaerts A, Depla D and Ignatova V 2003 *Nucl. Instruments Methods Phys. Res. Sect. B Beam Interact. with Mater. Atoms* **207** 415

[32] Güttler D, Abendroth B, Grötzschel R, Möller W and Depla D 2004 *Appl. Phys. Lett.* **85** 6134

[33] Depla D, Heirwegh S, Mahieu S and De Gryse R 2007 *J. Phys. D: Appl. Phys.* **40** 1957

[34] Vlček J and Burcalová K 2010 *Plasma Sources Sci. Technol.* **19** 065010

[35] Christie D J 2005 *J. Vac. Sci. Technol. A* **23** 330

[36] Rosén D, Katardjiev I, Berg S and Möller W 2005 *Nucl. Instruments Methods Phys. Res. Sect. B Beam Interact. with Mater. Atoms* **228** 193

[37] Eckstein W, Dohmen R, Mutzke A and Schneider R 2007 SDTrimSP: A Monte Carlo Code for Calculating Collision Phenomena in Randomized Targets (tech. report), Max-Planck-Institut für Plasmaphysik

[38] Depla D, Heirwegh S, Mahieu S, Haemers J and De Gryse R 2007 *J. Appl. Phys.* **101** 013301

[39] Kuschel T and Von Keudell A 2010 *J. Appl. Phys.* **107** 103302

[40] Lieberman M A and Lichtenberg A J 2005 *Principles of Plasma Discharges and Materials Processing: Second Edition* (New York: Wiley) ISBN 0471720011

[41] Vlček J, Pajdarová A D and Musil J 2004 *Contrib. to Plasma Phys.* **44** 426

[42] Kozák T and Pajdarová A D 2011 *J. Appl. Phys.* **110** 103303

[43] Huo C, Raadu M A, Lundin D, Gudmundsson J T, Anders A and Brenning N 2012 *Plasma Sources Sci. Technol.* **21** 045004

[44] Vitelaru C, Lundin D, Stancu G D, Brenning N, Bretagne J and Minea T 2012 *Plasma Sources Sci. Technol.* **21** 025010

[45] O'Hanlon J F 2005 *A User's Guide to Vacuum Technology* (Wiley) ISBN 0471467154

[46] Čapek J, Hála M, Zabeida O, Klemberg-Sapieha J E and Martinu L 2013 *J. Phys. D: Appl. Phys.* **46** 205205

[47] Lazar J, Vlček J and Rezek J 2010 *J. Appl. Phys.* **108** 063307

[48] Kozák T, Vlček J and Kos Š 2013 *J. Phys. D: Appl. Phys.* **46** 105203

[49] National Institute of Standards and Technology, Atomic Spectra Database, version 5 (accessed February 2015) `http://www.nist.gov/pml/data/asd.cfm`

[50] Britun N, Konstantinidis S and Snyders R 2015 *Plasma Process. Polym.* DOI: 10.1002/ppap.201500051

[51] Rossnagel S M 1988 *J. Vac. Sci. Technol. A* **6** 19

[52] Depla D and Mahieu S 2008 *Reactive Sputter Deposition* (*Springer Series in Materials Science* vol 109) (Berlin: Springer) ISBN 3540766642

[53] Pajdarová A D, Vlček J, Kudláček P and Lukáš J 2009 *Plasma Sources Sci. Technol.* **18** 025008

[54] Österlund L, Zoric I and Kasemo B 1997 *Phys. Rev. B* **55** 15452

[55] Anders A 2008 *Appl. Phys. Lett.* **92** 201501